Towards brain-wide noninvasive molecular imaging

by

Agata E. Wiśniowska

B.S. Physics, and
B.S. Nuclear Science and Engineering
Massachusetts Institute of Technology, 2011

Submitted to the Harvard-MIT Program in Health Sciences and Technology,
in partial fulfillment of the requirements for the degree of

Doctor of Philosophy in Medical Engineering and Medical Physics
at the
Massachusetts Institute of Technology

June 2019

Signature redacted

Signature of Author: _____
Harvard-MIT Program in Health Sciences and Technology
May 7, 2019

Signature redacted

Certified by: _____
Alan P. Jasanoff, PhD
Professor of Biological Engineering,
Nuclear Science and Engineering, and Brain and Cognitive Sciences
Thesis Supervisor

Signature redacted

Accepted by: _____
Emery N. Brown, MD, PhD
Director, Harvard-MIT Program in Health Sciences and Technology,
Professor of Computational Neuroscience and Health Sciences and Technology

Towards brain-wide noninvasive molecular imaging

by

Agata E. Wiśniowska

Submitted to the Harvard-MIT Program in
Health Sciences and Technology, in partial fulfillment of the
requirements for the degree of
Doctor of Philosophy
in Medical Engineering and Medical Physics

Abstract

An intricate interplay of signaling molecules underlies brain activity, yet studying these molecular events in living whole organisms remains a challenge. Magnetic resonance imaging (MRI) is the most promising imaging modality for development of molecular signaling sensors with deeper tissue penetration than optical imaging, and better spatial resolution and more dynamic potential in sensor design, compared to radioactive probes. MRI molecular sensors, however, have largely required micromolar concentrations to achieve detectable signals. In order to detect signaling molecules in the brain at their native low nanomolar concentrations, an improvement in MRI molecular sensors is necessary. Here we introduce a new *in vivo* imaging paradigm that uses vasoactive probes (vasoprobes) that couple molecular signals to vascular responses. We apply the vasoprobes to detect molecular targets at nanomolar concentrations in living rodent brains, thus satisfying the sensitivity requirement for imaging endogenous signaling events.

Even with more sensitive probes, molecular imaging of the brain is further complicated by the presence of the blood-brain barrier (BBB), designed by nature to protect this most vital of organs. We have therefore implemented a means to permit noninvasive delivery of imaging agents following ultrasonic BBB opening. We use the ultrasound technique to deliver another potent class of contrast agents, superparamagnetic iron oxides, and we show that effective permeation of brain tissue is achieved using this approach. We have also designed ultrasensitive vasoprobe variants designed to permeate the brain completely noninvasively, using endogenous transporter-mediated mechanisms. We present preliminary results based on this approach and discuss future directions.

Acknowledgements

I am very grateful to my advisor – Alan Jasanoff – for guiding me through this journey, for always finding time for insightful discussions and for challenging me to grow and become more confident as a researcher. I appreciate Alan finding wonderful people to join the lab, many of whom became dear friends and made this journey ever more delightful.

I appreciate my committee members – Elfar Adalsteinsson and Kwanghun Chung – always looking out for me and making me feel like they were 'on my side', as well as helping me see my research through a broader lens beyond molecular MRI.

I wanted to thank my academic advisor – Brett Bouma – for his support throughout my PhD with choosing classwork, research lab, and discussing career options afterwards.

I am deeply grateful to Robert Ohlendorf for being my close collaborator on the vasoprobe project (Chapter 2), for countless conceptual discussions, patience in waiting for *in vivo* results, and support in research-related endeavors and beyond.

I thank He Wei for producing large amounts of nanoparticles for the ultrasound project (Chapter 3), at times at short notice and for sharing his immense experience with nanoparticles.

I appreciate Adrian Slusarczyk teaching me most of what I know about protein engineering, cell culture, and molecular biology in general, and for being my collaborator on the delivery project (Chapter 4).

I whole-heartedly thank Mitul Desai for teaching me *in vivo* imaging techniques and data analysis, helping with countless troubleshooting, and being always ready to help even well after leaving MIT.

I am very grateful to Peter Harvey for collaboration on histological staining and microscopic imaging in Chapters 2 and 3, and for proofreading this thesis document.

I thank Lili Cai for helping me get started on the ultrasound project in the beginning of my PhD, and Ali Barandov for very quickly synthesizing neurotransmitter analogs used in Chapter 2.

Insightful discussions with Aviad Hai, Nan Li, Isabel Alvarez, Souparno Ghosh, Sarah Bricault, Ben Bartelle and Jacob Simon also have contributed to the success of this thesis work. I appreciate all the members of the Jasanoff lab for the countless lunches, coffee breaks, and leisure activities that we have shared.

I want to thank Atsushi Takahashi and Steven Shannon of the 9.4T imaging suite for always having a kind word and, occasionally, Nanuck to cuddle with.

I am grateful to Thalia Rubio at the writing and communication center for accompanying me on the journey of writing this document and preparing job applications last summer.

I want to thank Stanley and Connie Kowalski for being my 'grandparents' away from home, for their warmth, readiness to help, invitations for holiday celebrations, and ever-present kindness.

To my Chicago family – Gosia and my uncle – I'm grateful for frequent phone calls in the same time-zone, for knowing that I can always visit and for sharing this journey with me.

Finally, I thank my parents for always being there for me, supporting all my choices and endeavors, and for existing.

I thank my dog, known as Dryad, Driada, or dogwa, for her unparalleled unconditional love and affectionate licks no matter what.

Table of Contents

Chapter 1: Introduction

Currently, neuroscience faces the challenge of integrating the knowledge of cellular and molecular mechanistic information into the organism-wide study of brain function in behavior and cognitive processes. On the one hand, functional magnetic resonance imaging (fMRI)[1] enables noninvasive whole brain activity studies, but lacks the mechanistic information underlying the visualized brain activity. On the other hand, the reductionist neurobiology[2] approaches to structurally resolve neural networks are increasingly powerful yet typically invasive.

Molecular fMRI can bridge this gap by studying defined molecular signaling events over large regions of intact living brains[3,4]. The ability to detect individual molecular signaling targets would allow *in vivo* study of mechanistic information about cellular and molecular processes in whole living organisms, unlike fMRI where the readout is based on complex coupling of neuronal activity to blood flow changes[5]. Molecular fMRI readouts are equivalent to optical imaging agents like fluorescent dyes or proteins[6,7], but they influence magnetic signals instead of visible light, which makes them detectable in deep brain regions currently not achievable for optical tools. Hence, molecular fMRI can extend molecular mechanistic studies to intact living animals and may eventually allow mechanistic neuroimaging in humans.

There are two areas of growth for molecular fMRI: 1) increasing the number of physiological phenomena that can be studied by development of new and improvement of existing molecular probes, and 2) enabling noninvasive molecular fMRI by developing strategies for noninvasive brain-wide delivery of molecular probes. In the following

chapters of this thesis we address both of these areas, but first we provide some background on currently available molecular fMRI probes and strategies for their delivery to the brain.

Molecular fMRI probes

Here we summarize the existing state-of-the-art probes for calcium ions, neurotransmitters, and enzymes.

Calcium ions play an essential role in signal transduction and, as a result, have long been favored as a target for optical imaging and became one of the first targets for molecular fMRI probes. One class of calcium sensors is based on paramagnetic gadolinium, iron, or manganese building blocks that change their T_1-weighted enhancement properties upon calcium binding (Figure 1-1a). For example, a Gd^{3+}-based sensor displayed 10 μm calcium sensitivity *in vivo*[8] while a recent Mn^{3+}-based sensor was used to report on intracellular calcium fluctuations by MRI for the first time *in vivo*[9]. Another class of calcium sensors is based on superparamagnetic iron-oxide nanoparticles (SPIONs). In this approach, nanoparticles interact with calcium-binding proteins (Figure 1-1b) and produce a T_2-weighted signal enhancement upon calcium binding[10,11]. This technique was recently demonstrated in living rodent brains[12].

Expanding the menu of potential molecular targets available to image and associated with brain activity is a major goal for molecular fMRI. Neurotransmitters are of particular importance as they are directly involved in, and often regulate, neuronal signaling. So far, paramagnetic metalloprotein domains have been used to map dopamine release patterns following rewarding stimulation[13] (Figure 1-1c) and to

measure changes in serotonin reuptake in response to antidepressants[14] in living rodent brains. However, in general metalloprotein-based MRI sensors have to be applied at a minimum of 10 μM concentration to achieve detectable MRI signal change *in vivo*.

Subsequent work has focused on circumventing this inherent requirement for high concentration of the sensor by tapping into the endogenous contrast already available in vasculature. The concentration requirement is lowered by coupling molecular events to vascular responses: for example 100 nM of the vasoactive peptide, called calcitonin gene reported receptor (CGRP), -based sensor triggered fMRI response upon sensing enzymes in living rodent brains[15] (Figure 1-1d-e).

In this thesis we expand the vasoactive peptide sensor to localize implanted targets at nanomolar concentrations in living rodent brains and show utility of two other

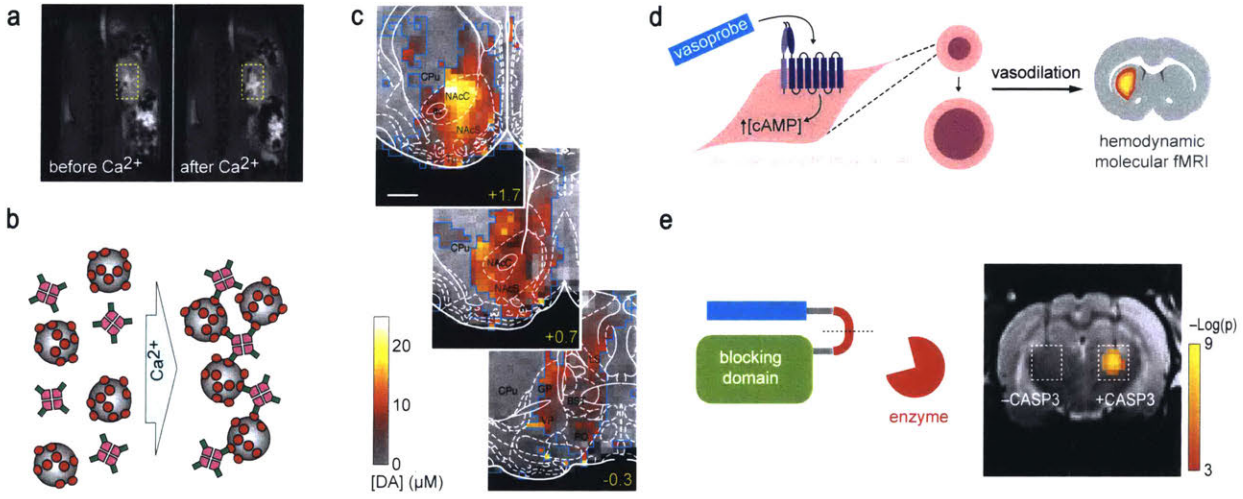

Figure 1-1. Molecular fMRI probes. **a**: MRI contrast change in a calcium sensor infused mouse kidney before vs after I.V. injection of $CaCl_2$. **b**: Mechanism of SPIONs clustering in the presence of calcium[10]. **c**: Quantitative mapping of dopamine release following rewarding stimulation in rat brain[13], scale bar = 2mm. **d**: Strategy for coupling molecular signals to vascular responses. **e**: Mechanism to utilize vasoprobes for enzyme detection and *in vivo* detection of caspase-3 at nanomolar concentrations[15].
Note: figure adapted from Ghosh et al 2018[3] with author's permission.

vasoactive probes: pituitary adenylate cyclase-activating polypeptide (PACAP) and Maxadilan as additional platforms for vasoprobe-based sensing (Chapters 2 and 4).

Strategies for noninvasive brain delivery

To enable whole brain molecular fMRI studies in animals and potential translation of mechanistic neuroimaging to humans, noninvasive delivery to the entire brain must be possible. Nature seems to be working against us in this aspect, protecting the brain as a vital organ with brain vasculature lined with the blood-brain barrier (BBB), which is composed of tight junctions between the endothelial cells lining the vessels to prevent potentially damaging substances in the blood from entering the brain[16,17]. Various strategies have been developed for transporting sensors across the BBB in a noninvasive way.

One of the most prominent and well-studied approaches is to transiently open the BBB using ultrasound waves following I.V. administration of microbubbles[18] (Figure 1-2a). The BBB stays open for >1h following its ultrasound-mediated opening. Various sized entities[19] have been successfully delivered to the brain using this approach, including paramagnetic agents (e.g. gadolinium)[20], genetically-encoded vectors[21–23], stem cells[24], and chemotherapeutic agents[25–27]. The potential for ultrasound-mediated BBB disruption extends to humans as recent clinical trials demonstrated successful delivery of chemotherapeutics in brain tumor patients[28]. Furthermore, the clinical trials for BBB opening in Alzheimer's patients[29] are underway and could extend the use of this technique to other neurological disorders.

An even safer approach is to rely on probes that cross the BBB on their own.

Spontaneously crossing agents predominantly make use of one of the three pathways through the BBB available (Figure 1-2b): 1) passive transport, 2) carrier mediated transcytosis, or 3) receptor mediated transcytosis (RMT). Passive transport requires small size of the probes (<400 daltons) and lipophilic properties[30], precluding most of the molecular probes from being good candidates for this route of transport. Receptor mediated transcytosis is of particular interest as a potential delivery platform of molecular sensors to the brain. In this mechanism an antibody that binds a BBB-crossing receptor is often referred to as a 'trojan horse'[31] because the antibody is recognized by the BBB as a BBB-crossing entity and yet these antibodies can carry substances into the brain that would not otherwise be permitted to enter. Trojan horses can carry large cargo across the BBB making them particularly attractive for molecular fMRI. Multiple trojan horse receptors have been identified and extensively tested, including transferrin receptor[32], insulin receptor[33], and a promising FC5 transporter[34].

RMT generally suffers from low dose delivered (<1% of injected dose) to the brain compared to the total dose injected intravenously (I.V.). As a result, sensors that function at low concentrations are particularly well-suited for this delivery method, such as the aforementioned vasoprobes that function at nanomolar concentration *in vivo*.

In this thesis we utilize the ultrasound-mediated BBB opening combined with particularly small SPIONs to achieve wide-spread delivery to brain parenchyma (Chapter 3), and we explore loading vasoprobes as a cargo in RMT and using their nanomolar potency as a potential readout of BBB crossing (Chapter 4).

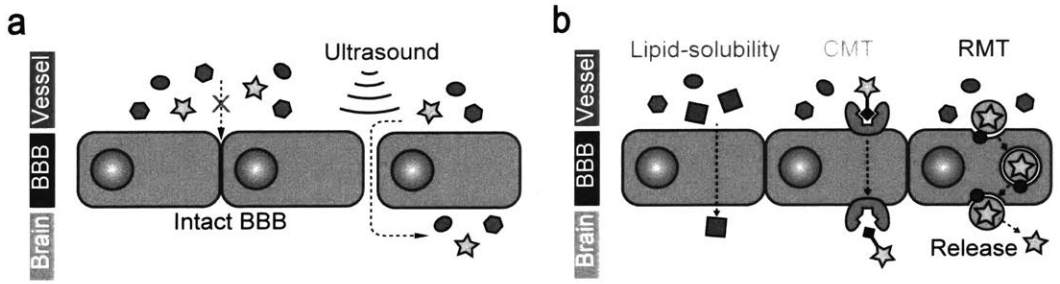

Figure 1-2. Strategies for delivery across the BBB. **a**: Schematic of transient ultrasound-mediated BBB opening. **b**: Schematic of endogenous transport mechanisms across the BBB; CMT- carrier mediated transcytosis, RMT-receptor mediated transcytosis.
Note: figure adapted from Ghosh et al 2018[3] with author's permission.

Conclusion

Molecular fMRI has the potential to provide mechanistic information in living intact organisms. The translation of this technique to humans will likely be driven by clinical needs. Overcoming the challenge of noninvasive delivery to the brain would make molecular fMRI a great technique for spatiotemporally resolved studies of diverse molecular events. The diagnostic applications of molecular fMRI could be envisioned for calcium signaling abnormalities implicated in autism and Alzheimer's disease[36,37], and neurotransmitter sensors could evaluate therapy outcomes for disorders that affect specific neurochemical systems e.g. Parkinson's disease or major depression. Molecular fMRI can definitely help us understand mechanistic processes in whole animal organisms and, we envision, someday could bring mechanistic neuroimaging to the clinical setting as a companion diagnostic[38] to access efficacy of drugs in treatment of neurological disorders.

References

1. Ugurbil, K. What is feasible with imaging human brain function and connectivity using functional magnetic resonance imaging. *Philos. Trans. R. Soc. Lond. B. Biol. Sci.* **371**, (2016).
2. Jorgenson Lyric A. *et al.* The BRAIN Initiative: developing technology to catalyse neuroscience discovery. *Philos. Trans. R. Soc. B Biol. Sci.* **370**, 20140164 (2015).
3. Ghosh, S., Harvey, P., Simon, J. C. & Jasanoff, A. Probing the brain with molecular fMRI. *Curr. Opin. Neurobiol.* **50**, 201–210 (2018).
4. Bartelle, B. B., Barandov, A. & Jasanoff, A. Molecular fMRI. *J. Neurosci.* **36**, 4139–4148 (2016).
5. Hillman, E. M. C. Coupling mechanism and significance of the BOLD signal: a status report. *Annu. Rev. Neurosci.* **37**, 161–181 (2014).
6. Lin, M. Z. & Schnitzer, M. J. Genetically encoded indicators of neuronal activity. *Nat. Neurosci.* **19**, 1142–1153 (2016).
7. Chen, T.-W. *et al.* Ultrasensitive fluorescent proteins for imaging neuronal actI.V.ity. *Nature* **499**, 295–300 (2013).
8. Moussaron, A. *et al.* Ultrasmall Nanoplatforms as Calcium-Responsive Contrast Agents for Magnetic Resonance Imaging. *Small Weinh. Bergstr. Ger.* **11**, 4900–4909 (2015).
9. Barandov, A. *et al.* Sensing intracellular calcium ions using a manganese-based MRI contrast agent. *Nat. Commun.* **10**, 897 (2019).
10. Atanasijevic, T., Shusteff, M., Fam, P. & Jasanoff, A. Calcium-sensitive MRI contrast agents based on superparamagnetic iron oxide nanoparticles and calmodulin. *Proc. Natl. Acad. Sci.* **103**, 14707–14712 (2006).
11. Rodriguez, E., Lelyveld, V. S., Atanasijevic, T., Okada, S. & Jasanoff, A. Magnetic nanosensors optimized for rapid and reversible self-assembly. *Chem. Commun.* **50**, 3595–3598 (2014).
12. Okada, S. *et al.* Calcium-dependent molecular fMRI using a magnetic nanosensor. *Nat. Nanotechnol.* **13**, 473 (2018).
13. Lee, T., Cai, L. X., Lelyveld, V. S., Hai, A. & Jasanoff, A. Molecular-Level Functional Magnetic Resonance Imaging of Dopaminergic Signaling. *Science* **344**, 533–535 (2014).
14. Hai, A., Cai, L. X., Lee, T., Lelyveld, V. S. & Jasanoff, A. Molecular fMRI of Serotonin Transport. *Neuron* **92**, 754–765 (2016).
15. Desai, M., Slusarczyk, A. L., Chapin, A., Barch, M. & Jasanoff, A. Molecular imaging with engineered physiology. *Nat. Commun.* **7**, 13607 (2016).
16. Daneman, R. & Prat, A. The blood-brain barrier. *Cold Spring Harb. Perspect. Biol.* **7**, a020412 (2015).
17. Pardridge, W. M. CSF, blood-brain barrier, and brain drug delivery. *Expert Opin. Drug Dell.V..* **13**, 963–975 (2016).
18. Aryal, M., Arvanitis, C. D., Alexander, P. M. & McDannold, N. Ultrasound-mediated blood-brain barrier disruption for targeted drug delivery in the central nervous system. *Adv. Drug Dell.V.. Rev.* **72**, 94–109 (2014).

19. Choi, J. J., Wang, S., Tung, Y.-S., Morrison, B. & Konofagou, E. E. Molecules of various pharmacologically-relevant sizes can cross the ultrasound-induced blood-brain barrier opening in vivo. *Ultrasound Med. Biol.* **36**, 58–67 (2010).
20. Hynynen, K., McDannold, N., Sheikov, N. A., Jolesz, F. A. & Vykhodtseva, N. Local and reversible blood–brain barrier disruption by noninvasive focused ultrasound at frequencies suitable for trans-skull sonications. *NeuroImage* **24**, 12–20 (2005).
21. Hsu, P.-H. *et al.* Noninvasive and Targeted Gene Delivery into the Brain Using Microbubble-Facilitated Focused Ultrasound. *PLOS ONE* **8**, e57682 (2013).
22. Huang, Q. *et al.* Targeted gene delivery to the mouse brain by MRI-guided focused ultrasound-induced blood–brain barrier disruption. *Exp. Neurol.* **233**, 350–356 (2012).
23. Thévenot, E. *et al.* Targeted Delivery of Self-Complementary Adeno-Associated Virus Serotype 9 to the Brain, Using Magnetic Resonance Imaging-Guided Focused Ultrasound. *Hum. Gene Ther.* **23**, 1144–1155 (2012).
24. Burgess, A. *et al.* Targeted Delivery of Neural Stem Cells to the Brain Using MRI-Guided Focused Ultrasound to Disrupt the Blood-Brain Barrier. *PLOS ONE* **6**, e27877 (2011).
25. Kinoshita, M., McDannold, N., Jolesz, F. A. & Hynynen, K. Noninvasive localized delivery of Herceptin to the mouse brain by MRI-guided focused ultrasound-induced blood–brain barrier disruption. *Proc. Natl. Acad. Sci.* **103**, 11719–11723 (2006).
26. Treat, L. H. *et al.* Targeted delivery of doxorubicin to the rat brain at therapeutic levels using MRI-guided focused ultrasound. *Int. J. Cancer* **121**, 901–907 (2007).
27. Poon, C., McMahon, D. & Hynynen, K. Noninvasive and targeted delivery of therapeutics to the brain using focused ultrasound. *Neuropharmacology* **120**, 20–37 (2017).
28. Carpentier, A. *et al.* Clinical trial of blood-brain barrier disruption by pulsed ultrasound. *Sci. Transl. Med.* **8**, 343re2 (2016).
29. Lipsman, N. *et al.* Blood–brain barrier opening in Alzheimer's disease using MR-guided focused ultrasound. *Nat. Commun.* **9**, 2336 (2018).
30. Banks, W. A. Characteristics of compounds that cross the blood-brain barrier. *BMC Neurol.* **9**, S3 (2009).
31. Pardridge, W. M. Re-engineering biopharmaceuticals for delivery to brain with molecular Trojan horses. *Bioconjug. Chem.* **19**, 1327–1338 (2008).
32. Yu, Y. J. *et al.* Therapeutic bispecific antibodies cross the blood-brain barrier in nonhuman primates. *Sci. Transl. Med.* **6**, 261ra154 (2014).
33. Boado, R. J., Ka-Wai Hui, E., Zhiqiang Lu, J. & Pardridge, W. M. Insulin receptor antibody-iduronate 2-sulfatase fusion protein: pharmacokinetics, anti-drug antibody, and safety pharmacology in Rhesus monkeys. *Biotechnol. Bioeng.* **111**, 2317–2325 (2014).
34. Farrington, G. K. *et al.* A novel platform for engineering blood-brain barrier-crossing bispecific biologics. *FASEB J. Off. Publ. Fed. Am. Soc. Exp. Biol.* **28**, 4764–4778 (2014).
35. Koffie, R. M. *et al.* Nanoparticles enhance brain delivery of blood-brain barrier-impermeable probes for in vivo optical and magnetic resonance imaging. *Proc. Natl. Acad. Sci. U. S. A.* **108**, 18837–18842 (2011).

36. Krey, J. F. & Dolmetsch, R. E. Molecular mechanisms of autism: a possible role for Ca2+ signaling. *Curr. Opin. Neurobiol.* **17**, 112–119 (2007).
37. Berridge, M. J. Calcium regulation of neural rhythms, memory and Alzheimer's disease. *J. Physiol.* **592**, 281–293 (2014).
38. Van Heertum, R. L., Scarimbolo, R., Ford, R., Berdougo, E. & O'Neal, M. Companion diagnostics and molecular imaging-enhanced approaches for oncology clinical trials. *Drug Des. Devel. Ther.* **9**, 5215–5223 (2015).

Chapter 2: Target-responsive vasoactive probes for ultrasensitive molecular imaging

Introduction

All biological processes depend on the action of numerous small molecules that coordinate communication and metabolism across multiple spatial and temporal scales. By mapping such species with minimal invasiveness in whole living organisms, molecular imaging could provide insight into diverse physiological functions and their disruption in disease. Fluorescent sensors are commonly used to monitor molecular processes at high resolution *in vivo*, but detection of fluorescent probes in most organisms is limited to superficial regions by optical scattering and absorption[1,2]. Sensitive detection of probes at subnanomolar concentrations in deep tissue is possible using nuclear imaging, but analyte-responsive probes for nuclear techniques are not available, so these methods can only measure localization and kinetics of the tracers themselves[3,4]. Magnetic resonance imaging (MRI) contrast agents are detectable in deep tissue, and can be sensitized to a variety of biologically-relevant targets. However, imaging agents for MRI are usually only detectable at micromolar concentrations, or at similar mass doses when nanoparticle contrast agents are used. This creates challenges for delivery of the probes, increases the potential for physiological disruptions or toxicity, and often means that only high analyte levels can be detected.

Vasoactive probes (vasoprobes) are a new class of imaging agent that could address the challenge of achieving sensitive detection of analytes in deep tissue with noninvasive detection at an organ- or organism-wide scale. Effective vasoprobes can be

derived from potent vasodilatory peptides that induce relaxation of the smooth muscle cells that surround most blood vessels (VSMCs). This in turn leads to spatiotemporally localized changes in blood flow, volume, and oxygenation that can be sensitively detected by a variety of imaging techniques, including MRI[5], ultrasound[6], nuclear imaging[7], and optical methods[8]. Recent results show that vasoprobes can be detected at nanomolar concentrations in the rodent brain, and that both secretion and proteolytic uncaging of vasoprobes give rise to specific signatures in imaging[9]. We therefore reasoned that the vasoprobe contrast mechanism could also be harnessed to create sensors for biologically-important molecules, and that target-responsive vasoprobes could facilitate detection of molecular species at the nanomolar concentrations characteristic of many signaling molecules, biochemical markers, and therapeutic agents.

Here, we develop a vasoprobe-based strategy for sensing small molecules by hemodynamic imaging *in vivo*. We engineer suitable imaging agents with the aid of a cell-based *in vitro* bioassay, and show that the resulting probes permit target-activated detection of nanomolar-scale molecular ligands in live rat brains. We focus initially on detection of biotin and biotinylated targets, but further demonstrate the generality of our design by tuning it for detection of an important neurotransmitter – dopamine, thus indicating the potential of vasoprobe technology for studying a wide variety of molecular phenomena in the brain and other organs.

Results

Note: *In vitro* vasoprobe engineering and optimization were performed by Dr. Robert Ohlendorf, the neurotransmitter construct synthesis was done by Dr. Ali Barandov, and the imaging of histological slices was done in collaboration with Dr. Peter Harvey.

Platform for vasoactive sensor construction

We chose to derive ligand-sensitive vasoprobes from the potent vasodilator pituitary adenylate cyclase-activating polypeptide (PACAP), a 38-residue peptide that activates G protein-coupled receptor-dependent cyclic adenosine monophosphate (cAMP) signaling in VSMCs with half-maximal effective doses (EC_{50}) in the sub-nanomolar range[10] (Figure 2-1a). Although PACAP is also involved in additional biological processes, the subtlety of PACAP knockout phenotypes[11] suggests that transiently applied PACAP-derived vasoprobes are unlikely to produce substantial physiological side-effects. The fact that PACAP lacks disulfide bonds also makes it more amenable to molecular bioengineering efforts than calcitonin gene-related peptide, which was used for initial demonstrations of the vasoprobe principle[9] but contains two disulfide bonds.

Our goal was to bring about PACAP-dependent hemodynamic image contrast that is activated only in the presence of target molecules. To that end, we envisioned a design wherein a PACAP derivative is labeled with a tethered version of the target molecule of interest, which in turn interacts with a protein domain that selectively binds either the tethered target or the target molecule itself in competition (Figure 2-1b). In the absence of the target molecule, the protein domain would remain bound to the PACAP moiety via

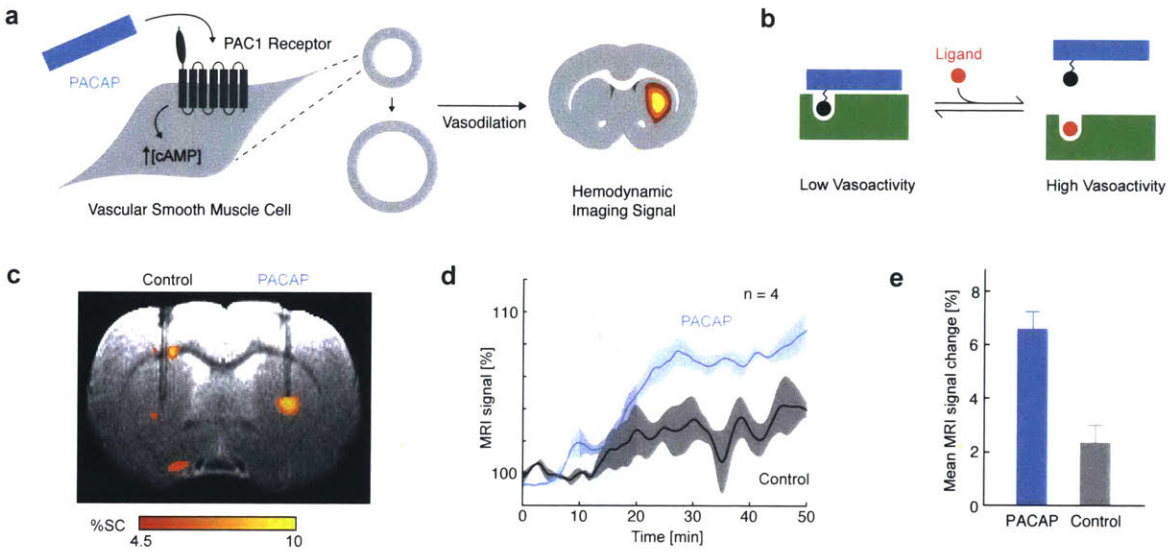

Figure 2-1. Platform for vasoactive sensor construction. **a**: Strategy for coupling PACAP activity to hemodynamic imaging signals. **b**: Schematic of PACAP-dependent vasoactivity, activated only in the presence of target ligands. **c**: Map of group MRI signal change following intracranial delivery of 1 μM PACAP compared to control, n=4, overlayed on an anatomical image. **d**: Group time course from the region underneath the cannula tip following intracranial delivery of 1 μM PACAP compared to control, n=4. **e**: Mean MRI signal change in the regions underneath the cannula tip after the plateau has been reached, n=4.

the tethered ligand, blocking PACAP from activating its receptors. The presence of elevated concentrations of the target molecule in tissue, however, would cause release of the PACAP derivative from the blocking protein, uncaging its bioactivity and evoking a local hemodynamic imaging signal.

To verify that PACAP could be a suitable basis for constructing such sensors, we first examined whether this peptide could function as an effective vasoprobe in the living rat brain (Figure 2-1c). Intracranial delivery of 1 μM PACAP caused a hemodynamic blood oxygenation level-dependent (BOLD) signal change of 6.6 ± 0.7% in T_2* relaxation-weighted MRI compared to only 2.3 ± 0.7% in response to control injections of artificial cerebrospinal fluid (CSF) vehicle (Figure 2-1d-e). Furthermore, PACAP-dependent responses could be visualized over multiple sequential blocks of injection (data not

shown). These results suggested that PACAP can indeed function as a platform for ligand-dependent vasoactive sensor design.

Engineering a vasoactive sensor

To demonstrate the PACAP-based vasoactive sensor principle, we decided initially to construct a sensor for the small molecule biotin. As biotin is widely used as a labeling moiety, a vasoactive biotin sensor would be immediately useful as a means of detecting endogenously or exogenously biotin-labeled species in tissue, thus acting as an *in vivo* analog of widely-used histological approaches. With a molecular weight of 244 Da, biotin is similar in size and characteristics to many endogenous signaling molecules and metabolites, so we anticipated that an imaging sensor for biotin could subsequently be adapted for detection of other small molecule targets. The tetrameric 53 kDa protein streptavidin (SA) and its close relatives bind tightly to both free and functionalized biotin derivatives[12], and are obvious candidates to act as blocking domains for a sensor constructed according to the design of Figure 2-1b.

The proposed sensor design requires site-specific tethering of biotin to PACAP in a way that (1) does not severely interfere with receptor activation, (2) allows for binding of the blocking protein domain, and (3) results in a sufficient activity change between blocked and unblocked states, such that substantial vasodilation occurs only in the unblocked state. We used a combination of structural data[13] and previous structure-function analysis results to identify candidate biotin attachment sites likely to satisfy these criteria (Figure 2-2b). A set of PACAP derivatives was prepared, for which each of these sequence positions was replaced with a lysine-biotin residue.

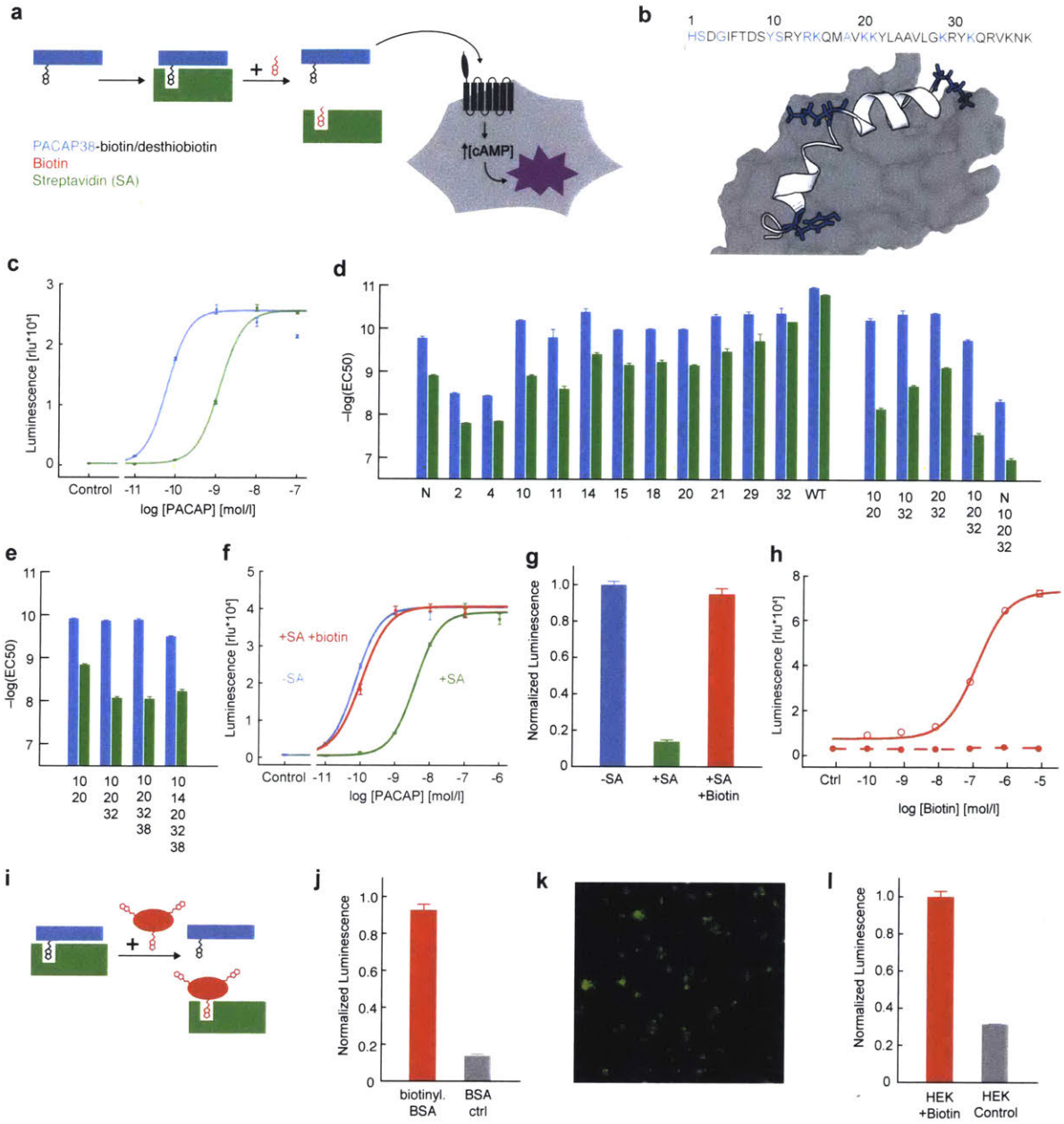

Figure 2-2. Engineering of biotin vasosensor. **a**: A luminescence cell assay where activation of PACAP receptor PAC1 results in a luminescence readout allowing screening of numerous target-activated sensor variants. **b**: Sequence of PACAP38 and structure of truncated PACAP(6-38) bound to the extracellular domain of PACAP receptor PAC1. Tested biotinylation sites are highlighted in blue in the peptide sequence and blue-highlighted residues in the structure indicate biotinylation/desthiobiotinylation sites in the final biotin vasosensor. **c**: Luminescence assay titration of PACAP38-Y10K-biotin in the presence (green) or absence (blue) of excess streptavidin (200 nM). **d**: *In vitro* screen for identifying PACAP residues that tolerate modification. Half-effective doses (EC_{50}) of PACAP-biotin conjugates (blue) and quantitative blocking by streptavidin (green). EC_{50} values derive from titrations as shown in panel c. **e**: Testing streptavidin-mediated blocking of PACAP38-desthiobiotin conjugates. EC_{50} in the presence (green) and absence (blue) of streptavidin. **f**: Titration curves of biotin vasosensor (PACAP38-10-20-32-desthiobiotin) in the absence (blue) and presence (green) of 200 nM streptavidin, and upon addition 8 μM biotin (red). **g**: Data for 1 nM biotin vasosensor from panel f. The vasosensor (blue) gets blocked by streptavidin (green) and gets released by free biotin (red). **h**: Titration of blocked biotin vasosensor (1 nM PACAP38-10-20-32-desthiobiotin + 2 nM streptavidin) by biotin (solid line) showing activation with EC_{50} of 120 ± 10 nM. An equivalent biotinylated variant of the sensor (broken line) does not get activated by free biotin. **i**: Vasosensor activation by biotinylated targets. **j**: Biotin vasosensor activation by biotinylated protein target (BSA). **k**: Fluorescence image showing biotinylated HEK cells stained with fluorescent streptavidin. **l**: Biotin vasosensor activation by biotinylated HEK cells corresponding to 50 nM biotin.

To rapidly screen these variants, we established a luminescence assay in mammalian cells that models PACAP-related vasoactivity by quantitatively reporting cAMP production in response to activation of the PACAP receptor PAC1 (Figure 2-2a). Titration of PACAP derivatives in this assay enabled EC_{50} values to be obtained for each variant, in both the presence and absence of SA (Figure 2-2c-d). With the exception of several residues near the N-terminus, biotinylation of most PACAP residues is well tolerated in the absence of SA, with variants displaying EC_{50} values only modestly lower than the value exhibited by wild-type PACAP (Figure 2-2d). Losses of potency by ~300-fold upon biotinylation of positions 2-5 is consistent with previous studies reporting the requirement for these residues in receptor activation[10,13].

Addition of SA to the biotinylated PACAP variants produces variable effects on bioactivity. Residues close to the C-terminus that tolerate biotinylation well show only modest activity reduction upon SA addition. Similarly, PACAP variants biotinylated near the N-terminus that already show low activity are only slightly further compromised by addition of SA. Among the tested residues, biotinylation of sites in the mid-region of the peptide produced the greatest SA-dependent dynamic range in receptor activation. In particular, a PACAP variant biotinylated at residue Y10 (PACAP-10-BT) provides the best combination of preserved bioactivity and sensitivity to SA binding.

We wondered whether residual bioactivity of PACAP-10-BT in the presence of SA is due to incomplete binding of SA or to the presence of a minor unbiotinylated PACAP population that fails to bind SA even in the presence of excess protein. We sought to improve availability of biotin to SA binding by extending the linker between biotin and the PACAP backbone at position 10, but this had no apparent effect on SA-mediated blocking

in the receptor activation assay (data not shown). We also repurified PACAP-10-BT in an attempt to further deplete unbiotinylated peptide contaminants, but found no effect on the peptide's EC_{50} in the presence of SA. On the other hand, biotinylating PACAP at residue 20 along with residue 10 produced a variant, PACAP-10,20-BT, with reduced potency in the presence of SA, suggesting that further occlusion of the receptor-binding interface is the key to improving the SA-dependent dynamic range of PACAP derivatives. PACAP-10,20-BT displays an EC_{50} of 61 ± 7 pM that is reduced by a factor of 115 ± 22 in the presence of SA (Figure 2-2d). Addition of further PACAP biotinylation sites did not substantially improve on these properties.

Detecting biotin with nanomolar sensitivity *in vitro*

The combination of PACAP-10,20-BT and SA could in principle function as a vasoprobe-based biotin sensor, but the characteristic dissociation time of SA from biotin is too long for meaningful applications based on the competition principle of Figure 2-1a. To achieve effective biotin sensing, we therefore replaced the tethered biotin residues in PACAP-10,20-BT with desthiobiotin, a similar compound that binds SA with 10,000-fold lower affinity[14] than biotin and can be easily displaced by it[15]. The resulting peptide, PACAP-10,20-dBT, is not as effectively blocked by SA as PACAP-10,20-BT, but addition of further biotinylation sites addressed this problem (Figure 2-2e). A variant in which tethered desthiobiotins were attached at positions 10, 20, and 32 proved optimal; displaying a robust 63-fold difference in potency we expected would be suitable for biotin sensing.

A functional vasoprobe-based sensor for biotin (VS-BT) was formed by mixing 1 nM PACAP-10,20-32-dBT with two-fold molar excess of SA (Figure 2-2f-g). Titration of this sensor with varying amounts of biotin in the PAC1 bioassay reveals an EC_{50} for biotin detection of 120 ± 10 nM (Figure 2-2h). This range is sensitive enough to detect typical biotinylation levels associated with biotin display or labeling technologies, but not so sensitive as to be triggered by endogenous plasma biotin levels. The response of VS-BT to biotin reaches steady state quickly, and is reversible over repeated cycles of excess SA and biotin addition (data not shown).

To test functionality of VS-BT in more naturalistic contexts, we used the PAC1 bioassay to evaluate the sensor's *in vitro* responses to biotin moieties immobilized on molecules and cells. Bovine serum albumin (BSA) was treated with *N*-hydroxysuccinimidobiotin (NHS-biotin) to prepare a representative protein-conjugated target containing biotin. When challenged with this target, VS-BT produces a strong response, exhibiting a robust change in PAC1 receptor activation, which is not produced by BSA alone (Figure 2i-j). A cellular target containing 50 nM biotin was similarly prepared by treating HEK293 cells with NHS-biotin. This target elicits a 70% change in VS-BT bioactivity, compared with untreated HEK cells, according to the receptor activation assay (Figure 2k-l). These results show that VS-BT maintains sensitivity and selectivity for biotin even in biological environments, suggesting the suitability of vasoprobe-based sensors for applications *in vivo*.

Ultrasensitive vasoprobe-based molecular imaging *in vivo*

Biotin is widely used as a labeling agent *in vivo*, and an effective biotin sensor could be used to map the location and dynamics of biotinylated cells and molecules in living organisms. To evaluate this approach, we implanted biotinylated and nonbiotinylated cells into rat cortex and performed molecular imaging of these targets using VS-BT (Figure 2-3a). In order to survey a large region of the brain with minimal invasiveness, including but not limited to the cell implantation site, the vasoprobe was infused into the CSF at the rostral extent of the cortex. Spreading of imaging agents introduced using this route was verified by injecting the conventional contrast agent gadolinium diethylenetriaminepentaacetic acid (Gd-DTPA) and then visualizing the results by T_1-weighted imaging. Indeed, a volume of 40 μL of 200 mM Gd-DTPA produced strong spread throughout the anterior quadrant of the brain, enhancing contrast across a large volume including the cell implantation site, as well as additional regions of the olfactory bulb, frontal cortex, prelimbic cortex, motor cortex, and cingulate cortex (Figure 2-3b).

In the area of the implanted cells, VS-BT produces MRI readouts with BOLD contrast that clearly distinguishes biotinylated from control xenografts (Figure 2-3d-g). Comparison of histological results with vasoprobe-based images from individual animals confirms colocalization of the VS-BT-mediated signal with the biotin-containing xenografts (Figure 2-3c). Estimation of biotin content in the test cell implants indicates that biotin concentrations of about 50 nM were present, far below analyte levels detectable by conventional paramagnetic MRI contrast agents. The data of Figure 3 thus

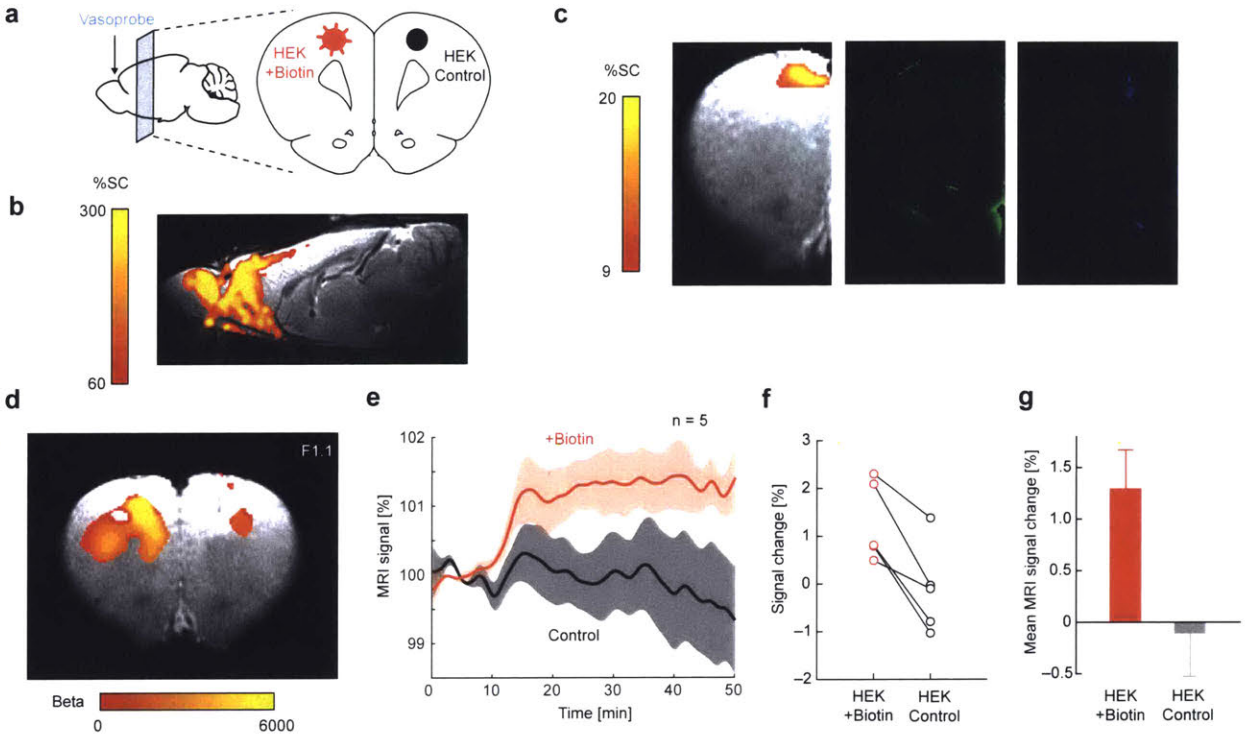

Figure 2-3. Ultrasensitive vasoprobe-based molecular imaging *in vivo*. **a**: Schematic of *in vivo* experimental design: distal vasoprobe delivery to bilaterally xenografted cells. **b**: Validation of CSF delivery technique via infusion of 200 mM of Gd-DTPA, the spread is visualized by signal change in T_1-weighted MRI overlayed on the anatomical image. **c**: Histological evidence of vasoprobe reaching xenografted cell populations; from left to right: MRI signal change overlayed on anatomical image, vasoprobe blocking domain streptavidin-DyLight 488 bound to xenografted biotinylated cells, and cell population localized by DAPI staining. **d**: Map of correlation beta coefficient matching signature of vasoactive probe MRI readout overlayed on the anatomical image; left: HEK+biotin, right: HEK-biotin, F statistic=1.1, n=5. **e**: Group time course from the region covered by xenografted cells following distal delivery of 2 μM vasoprobe compared to control, n=5. **f**: Consistent increase in MRI signal in each animal for biotinylated cells compared to control, n=5. **g**: Mean MRI signal change in the region covered by xenografted cells after the signal has stabilized, n=5.

demonstrate that nanomolar target concentrations can be imaged using VS-BT in conjunction with wide-field CSF delivery methods in rat brain.

Neurotransmitter-sensitive vasoprobe

The architecture of VS-BT could in principle be generalized for sensing a wide variety of small molecule targets. Neurochemicals are of particular interest because of

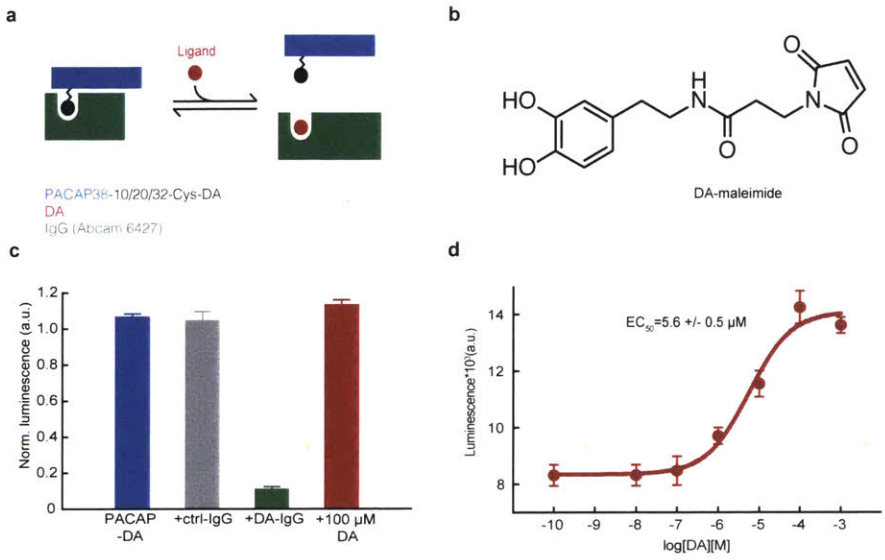

Figure 2-4. Neurotransmitter-sensitive vasoprobe. **a**: Design of dopamine vasosensor: PACAP38 is conjugated with tethered dopamine (see panel b) at residues 10, 20 and 32 and blocked by a dopamine-specific IgG antibody (green). Elevated concentrations of free dopamine (red) bind the antibody and release blocking. **b**: Structure of dopamine-maleimide compounds for labeling PACAP38 residues 10, 20 and 32 that were mutated to cysteine. **c**: Cell assay data showing activity of 1 nM dopamine vasosensor PACAP38-10-20-32-DA (blue). The presence of an unspecific control IgG antibody (600 nM) does not interfere with vasosensor activity, whereas 600 nM dopamine-specific IgG blocks the vasosensor (green). Excess of free dopamine (100 µM) fully activates the vasosensor (red). **d**: Dopamine activates dopamine vasosensor PACAP38-10-20-DA with EC_{50} of 5.6 ± 0.5 µM.

their distinct functional roles in the nervous system and their importance in health and disease. Although neurotransmitter sensors for MRI have been reported, they are not sensitive enough to report the submicromolar extracellular concentrations characteristic of many species.

To adapt the vasoprobe-based sensing mechanism for neurotransmitter detection, we mutated PACAP residues Y10, K20 and K32 to cysteines and conjugated the resulting thiol groups to synthetic thiol-reactive derivative of dopamine (DA) (Figure 2-4a-b). The conjugate showed EC_{50} values of 5.6 ± 0.5 µM for PAC1 receptor activation in the cell-based assay (Figure 2-4d), indicating that tolerance for modification of PACAP at the 10, 20, and 32 positions is general. Vasoprobe sensor for DA was formed by mixing the

modified peptides with immunoglobulins (IgGs) directed against the tethered neurotransmitter moieties, giving rise to the dopamine sensor VS-DA (Figure 2-4c). In this sensor, the IgGs function as protein blocking domains according to the design of Figure 2-1b, analogously to the SA component in VS-BT.

Discussion

Our work introduces target-responsive PACAP-based vasoprobes as a versatile platform for imaging small molecules in deep tissue with nanomolar sensitivity. Vasoprobe sensors are applied at concentrations more than 1,000-fold lower than conventional MRI agents and comparable to some nuclear imaging probes, making them particularly suitable for detection of the many biological targets that are present only at submicromolar concentrations *in vivo*. We designed the biotin-sensitive vasoprobe VS-BT, which is able to visualize biotin-labeled cell populations in MRI following wide-field delivery of the probe in live rat brains. Combined with *in vitro* or *in vivo*[16] biotinylation approaches, VS-BT could permit the mapping of target biomolecules or cell populations over time, using a variety of noninvasive imaging modalities. We demonstrate adaptability of the vasoprobe-based architecture by designing agents that detect single digit μM levels of the neurotransmitter DA. Incorporation of alternative tethered targets and cognate binding domains could permit a wide variety of further vasoprobe-based sensors to be constructed, in some cases leveraging well-characterized components of previously described fluorescent imaging probes[17–26].

The high sensitivity of vasoprobe-based agents for their targets arises in large part from their exploitation of physiological amplification pathways built into the vasculature. A

cost to this mechanism is that the results are not as easy to interpret quantitatively as imaging signals provided by simpler means, such as relaxation changes provided by conventional MRI contrast agents. Nevertheless, quantification of vasoprobe targets should be possible in contexts where calibration of vasoprobe-mediated signals can be performed as a function of known analyte concentrations. The PAC1 activation assay used here could provide an external standard for this; for instance, if we suppose that the biotin-triggered VS-BT responses of Figure 2-2f constitute about half the maximum response of ~20% observed in similar hemodynamic imaging experiments, then we would crudely but correctly infer that the amount of biotin detected approximately matches the *in vitro* EC_{50} of VS-BT for biotin. This external calibration approach could be improved by performing explicit measurements of maximal hemodynamic changes *in situ*, using established techniques. The best approach to quantification of vasoprobe sensor responses, however, would involve internal calibration using analyte standards applied in living control subjects.

The spatiotemporal properties of vasoprobe-based analyte sensing likewise follow largely from their unique hemodynamic mechanism. The probes are compatible with a variety of highly refined *in vivo* imaging methods, including magnetic, nuclear, ultrasonic, and optical approaches that in some cases provide spatial detail on the order of single blood vessels (< 100 μm). The temporal resolution of vasoprobe-based sensors is likely to be limited by hemodynamic response time courses on the order of seconds, and may be further limited by the kinetics of the competitive interactions between analytes and the blocking domains used in the vasoprobe sensor designs presented here. For neurotransmitter sensing, kinetic characteristics of vasoprobes may thus be comparable

to previous neurotransmitter-sensitive MRI probes, which display response time constants of tens of seconds; these are favorable with respect to receptor displacement strategies used in positron emission tomography, which generally require measurements lasting tens of minutes.

The sensor architecture we describe here entails the combination of ~5 kDa PACAP derivatives with proteins that range from 60 to 150 kDa in molecular weight. Even the largest of these has a hydrodynamic radius on the order of 5 nm, smaller than most nanoparticle-based imaging agents. The relatively small size and high potency of vasoprobe-based sensors should facilitate delivery of these probes to a variety of tissues in which they are predicted to elicit analyte-dependent hemodynamic responses. The brain is of particular interest because of its important chemical signaling systems and inaccessibility to most diagnostic agents. Interestingly, PACAP derivatives have been shown in earlier studies to spontaneously permeate the blood-brain barrier, suggesting the possibility of completely noninvasive delivery of PACAP-based sensors to the central nervous system. Although this avenue remains to be explored, the experiments presented here already demonstrate that vasoprobes can access large fields of view in the rodent brain following minimally-invasive intra-CSF infusion. Potent and responsive vasoprobe-based sensors, when applied using such delivery approaches, could thus provide unprecedented capability for monitoring small molecule targets throughout much of the body.

Methods

Peptide synthesis. Various PACAP-based constructs were designed by Dr. Robert Ohlendorf and synthetized and purified by Peptides and HPLC core at the Koch Institute for Integrative Cancer Research at MIT.

In vitro assessment of PACAP-based constructs. These methods were performed as previously described in Chapter 4 of Dr. Adrian Slusarczyk's thesis[27].

Preparation of neurotransmitter conjugates. The neurotransmitter, dopamine, was functionalized with a maleimido moiety to provide a facile and selective conjugation with specific amino acid sequence through the sulfhydryl groups of cysteins. Addition of the maleimido functional group was achieved by reacting dopamine with N-succinimidyl 3-maleimidopropionate in anhydrous dimethylformamide and further purification using high performance liquid chromatography (HPLC). The resulting functionalized neurotransmitter, DA-Mal, was reacted with specific amino acid sequence in PBS buffer (1X, pH 7.4) using an excess of DA-Mal (6 equiv.). The conjugate was purified by HPLC and its molecular structure was confirmed by high-resolution matrix assisted laser desorption/ionization mass spectrometry (MALDI-MS).

Animal procedures. All animal procedures were conducted in accordance with National Institutes of Health guidelines and with the approval of the MIT Committee on Animal

Care. All experiments were performed with male Sprague-Dawley rats, age 7–9 weeks, supplied by Charles River Laboratories (Wilmington, MA).

Magnetic Resonance Imaging (MRI). Seventeen Sprague-Dawley rats were used for *in vivo* MRI experiments. Data were acquired on a 7T 20 cm inner diameter, horizontal bore magnet (Bruker BioSpin MRI GmbH, Ettlingen, Germany) with surface and volume radiofrequency coils (Doty Scientific, Columbia, SC) positioned as described in the following sections.

Surgery for assessment of vasoactive probe injection. Four rats underwent surgery to implant bilateral cannula guides over the caudateputamen region of the striatum (CPu). The rats were induced using 3% isoflurane (ISO) anesthesia and maintained using 2% ISO with vacuum suction turned on to remove excess anesthetic. The rats were injected subcutaneously with 1.2 mg/kg of sustained release buprenorphine for analgesia. The rats' eyes were covered with paralube vet ointment (Dechra Veterinary Products, Overland Park, KS) to prevent eyes from drying from exposure to ISO. The rats' heads were shaved and cleaned with alcohol and povidone-iodine prep pads for easy access to the skull. Using sterile surgical equipment, the skin over the skull was retracted and the skull cleaned of tissue so that the sutures on the skull were clearly visible. The holes were drilled through the skull for the cannula guides bilaterally at 3 mm lateral to midline, 0.5 mm anterior from bregma. A small 26 GA needle was used to puncture the dura in each of the drilled holes, allowing smooth access to the brain parenchyma. The holes were air dried and bilateral connected custom-made cannula guides (22 GA PEEK, 6 mm distance

between the guides, Plastics One Inc, Roanoke, VA) were inserted into the holes. The guides were protruding 1 mm into the brain parenchyma. The guides were secured to the skull using white dental cement (C&B Metabond, Parkell, Edgewood, NY). Next, an in-house-made head post was attached to the rats' skulls posterior to the cannula guides implantation site using the white dental cement. After the cement dried, the pink cold cure dental cement (Teets Denture Material, Patterson Dental, Saint Paul, MN) was applied over the white cement to secure the entire implant. Tissue glue was applied to seal the surface connecting the cement and skin areas around the implant. Cannula guides were sealed with dummy cannulas (protruding as far as the guide) to avoid exposure of brain tissue during the recovery period.

MRI assessment of injected PACAP probes.

Experimental setup. Seven days after the implantation of the bilateral cannulas, four rats were imaged during PACAP intracranial infusion. For the imaging experiments, animals were anesthetized using 2% ISO in oxygen for induction. After numbing the trachea with lidocaine, the animals were intubated intratracheally using a 16 GA plastic part of the Surflash I.V. catheter (Terumo Medical Products, Somerset, NJ). The rats were then connected to a small animal respirator (Inspira Advanced Safety Ventilator; Harvard Apparatus, Holliston, MA), and fixed via their headposts into a custom built cradle for imaging with a commercial surface radiofrequency coil (Doty Scientific, Columbia, SC) fitting snugly around the headpost. Breathing rate and end-tidal expired isoflurane were continuously monitored. Once positioned in the cradle, the anesthesia was lowered to 0.75% ISO and the rats were paralyzed with pancuronium (1 mg/kg IP bolus for induction,

2 mg/kg/h IP infusion) to prevent motion artifacts during imaging. Immediately before each experiment, two injection internal cannulas, designed to protrude 4 mm into the brain past the cannula guides reaching into the CPu region of the striatum (28 GA PEEK internal cannula, Plastics One, Roanoke, VA, USA), were attached to 25 µl Hamilton glass syringes and prefilled with the appropriate intracranial injection solution (aCSF or 1 µM PACAP in aCSF). Injection cannulas were then lowered, while applying positive pressure of 0.01 µL/min to avoid air bubbles, into the previously implanted bilateral cannula guides. Next, the Hamilton syringes were placed in a remote infuse/withdraw dual syringe pump (PHD 2000 Syringe Pump; Harvard Apparatus, Holliston, MA). Animals with their radiofrequency (surface and volume) coils (Doty Scientific, Columbia, SC) were inserted into the magnet bore and locked in a position such that the head of the animal was at the center of the magnet bore.

MRI and data analysis. Animals were scanned by MRI to measure the changes in hemodynamic contrast following intracranial injections. High resolution T2-weighted anatomical scans of each animal were obtained using a rapid acquisition with relaxation enhancement (RARE) pulse sequence with echo time (TE) = 44 ms, repetition time (TR) = 2,500 ms, RARE factor 8, spatial resolution 100 µm x 100 µm x 1 mm, and matrix size 256 x 256 with seven slices. Hemodynamic contrast image series were acquired using a gradient echo planar imaging (EPI) pulse sequence with TE = 25 ms, TR = 2,000 ms, spatial resolution 390 µm x 390 µm x 1 mm, and matrix size 64 x 64 with seven slices. Ten minutes of baseline measurement with 4 s per time point were acquired before probe infusion. Following this baseline period, while continuously collecting EPI scans, the infusion pump was remotely turned on to commence intracranial injection (in the

parenchymal tissue) of 1 µl aliquots of 1 µM PACAP or control solutions at the rate of 0.1 µl/min through the cannulas. EPI scans continued being collected for 30 minutes after the infusion of the PACAP probe has stopped for the total scan time of 50 minutes. MRI data was processed and analyzed using the AFNI software. The AFNI 3dAllineate command was used to align each animal's EPI data set to the corresponding RARE anatomical image. Each animal's image data were then aligned to the cannula tip of a reference anatomical MRI. We scaled each animal's data assigning the mean of the baseline time period to 100 using AFNI's 3dcalc command. To identify voxels with significant increases or decreases in BOLD signal, we compared the signal of 10 minutes after the infusion to the baseline in the group concatenated data. For visualization, group signal change maps were overlaid on a reference anatomical image. Time courses were obtained by averaging MRI signal over 1.2 x 1.2 mm regions of interest defined around cannula tip locations in individual animals' datasets and standard error was calculated across animals using MATLAB. The plateau percent signal change was determined by comparing signal values during baseline and after the infusion conditions.

Preparation of cells for *in vivo* implantation. HEK293 Freestyle cells were separated into two 10 mL samples with 30 million cells/sample. The cells were washed twice with 10 mL ice cold PBS (pH 7.4) and resuspended in 1 mL each. The test sample was biotinylated by adding 120 µL of biotinylation reagent (EZ-link NHS-ester, ThermoFisher Scientific, Waltham, MA). 120 µL of PBS (pH 7.4) was added to the control cells. The cells were nutated for 30 minutes at room temperature and another 30 minutes at 4 °C. The cells were washed three times with ice cold PBS (pH 7.4) and resuspended in 100

μL of aCSF. The cells were biotinylated immediately before their implantation in a rat brain.

***In vivo* implantation of the cells and the distal delivery cannula for MRI imaging.** Five rats underwent surgery to implant the test and control cells bilaterally and to implant the distal delivery cannula at the rostral extent of the cortex (5.2 mm anterior from the bregma, on the midline). The rats were inducted using 3% isoflurane (ISO) anesthesia and maintained using 2% ISO with vacuum suction turned on to remove excess anesthetic. The rats' eyes were covered with paralube vet ointment (Dechra Veterinary Products, Overland Park, KS) to prevent eyes from drying from exposure to ISO. The rats' heads were shaved and cleaned with alcohol and povidone-iodine prep pads for easy access to the skull. The skin over the skull was retracted and the skull cleaned of tissue so that the sutures on the skull were clearly visible. Three holes were drilled through the skull: one for the distal injection just behind the olfactory bulbs (5.2 mm anterior from the bregma, on the midline), and two for the cell injections bilaterally 2 mm lateral to midline, 3.2 mm anterior from bregma. A small 26 GA needle was used to puncture the dura in each of the drilled holes, allowing smooth access to the brain parenchyma and the holes were air dried. Immediately before each experiment, two injection metal internal cannulas, designed to minimize damage caused to the brain tissue (33 GA, Plastics One, Roanoke, VA, USA), were attached to 25 μl Hamilton glass syringes and prefilled with the freshly biotinylated or control HEK cells. The injection cannula were then lowered 2mm into the brain parenchyma and 3 μL of the cell suspension (~0.5 million of cells) was injected over 30 minutes at a rate of 0.1 μL/min. After the cell injection was completed, the cannulae

were removed and the cell injection holes were dried and sealed with an SEcure Dual-Cure Resin Cement (Parkell Inc., Edgewood, NY). The cannula guide for the distal injection (22 GA PEEK, blunt, no protrusion into the brain parenchyma, Plastics One Inc, Roanoke, VA) was inserted into the most anterior hole. The guide was secured to the skull using white dental cement (C&B Metabond, Parkell, Edgewood, NY). Next, an in-house-made head post was attached to the rats' skulls posterior to the cannula guides implantation site using the white dental cement. After the cement dried, the pink cold cure dental cement (Teets Denture Material, Patterson Dental, Saint Paul, MN) was applied over the white cement to secure the entire implant. Tissue glue was applied to seal the surface connecting the cement and skin areas around the implant. The cannula guide was sealed with a dummy cannula (protruding as far as the guide) to avoid exposure of brain tissue before the MRI assessment.

MRI of gadolinium delivery.

The distal intra-CSF cannula guide and headpost were implanted as described above. One hour after the implantation of the distal delivery cannula, four rats were imaged during Gd-DTPA infusion through the distal intra-CSF cannula. Animals were anesthetized using 2% ISO in oxygen. After intubation, as described above, the rats were connected to a small animal respirator (Inspira Advanced Safety Ventilator; Harvard Apparatus, Holliston, MA), and fixed via their headposts into a custom built cradle for imaging with a commercial surface radiofrequency coil (Doty Scientific, Columbia, SC) fitting snugly around the headpost. Breathing rate and end-tidal expired isoflurane were continuously monitored. Immediately before each experiment, the internal cannula, designed to

protrude 0.25 mm past the CSF delivery cannula guide (28 GA PEEK internal cannula, Plastics One, Roanoke, VA, USA), was attached to 50 µl Hamilton glass syringe and prefilled with gadolinium T_1 agent (200 mM of Gd-DTPA in aCSF). The injection cannula was then lowered, while applying positive pressure of 0.1 µL/min to avoid air bubbles, into the previously implanted cannula guide. Next, the Hamilton syringe was placed in a remote infuse/withdraw dual syringe pump (PHD 2000 Syringe Pump; Harvard Apparatus, Holliston, MA). Animals with their radiofrequency (surface and volume) coils (Doty Scientific, Columbia, SC) were inserted into the magnet bore and locked in a position such that the head of the animal was at the center of the magnet bore. Animals were scanned by MRI to measure the extent of spread of the T_1 gadolinium agent throughout the brain. High resolution T_2-weighted anatomical scans of each animal were obtained using a rapid acquisition with relaxation enhancement (RARE) pulse sequence with TE = 44 ms, TR = 2,500 ms, RARE factor 8, spatial resolution 100 µm x 100 µm x 1 mm, and matrix size 256 x 256 with seven slices. T_1 contrast was monitored using T_1-weighted FLASH pulse sequence with TE = 5 ms, TR = 93.75 ms, spatial resolution 400 µm x 400 µm x 1 mm, and matrix size 64 x 64 with seven slices. Ten minutes of baseline measurement with 30 s long FLASH scan per time point were acquired before T_1 agent infusion. Following this baseline period, while continuously collecting FLASH T_1 scans, the infusion pump was remotely turned on to commence distal sensor injection (into the CSF) of 40 µl aliquot of 200 mM Gd-DTPA in aCSF at the rate of 1 µl/min through the distal delivery cannula. FLASH T_1 scans continued being collected for 10 minutes after the infusion of the T_1 agent has stopped for the total scan time of 60 minutes. MRI data was processed and analyzed using the AFNI software. Each animal's data was

normalized by assigning the mean of the baseline time period to 100% using AFNI's 3dcalc command. To identify voxels with significant increases or decreases in T_1 signal, the signal after the infusion was compared to the baseline in each animal. For visualization, a representative animal signal change map was overlaid on a reference sagittal anatomical image.

MRI of implanted cells.

Experimental setup. One hour after the implantation of the cells and the distal delivery cannula, five rats were imaged during caged PACAP-based biotin sensor intra-CSF infusion. For the imaging experiments, animals were anesthetized using 2% ISO in oxygen for induction. After numbing the trachea with lidocaine, the animals were intubated intratracheally using a 16 GA plastic part of the Surflash I.V. catheter (Terumo Medical Products, Somerset, NJ). The rats were then connected to a small animal respirator (Inspira Advanced Safety Ventilator; Harvard Apparatus, Holliston, MA), and fixed via their headposts into a custom-built cradle for imaging with a commercial surface radiofrequency coil (Doty Scientific, Columbia, SC) fitting snugly around the headpost. Breathing rate and end-tidal expired isoflurane were continuously monitored. Once positioned in the cradle, the anesthesia was switched to 0.05 mg/mL Dormitor mixed with 1 mg/mL pancuronium for paralysis (1 mL/kg IP bolus for induction, 2 mL/kg/h IP infusion afterwards) to prevent motion artifacts during imaging. Immediately before each experiment, the internal cannula, designed to protrude 0.25 mm past the CSF delivery cannula guide (28 GA PEEK internal cannula, Plastics One, Roanoke, VA, USA), was attached to 50 µl Hamilton glass syringe and prefilled with the caged PACAP-based biotin

sensor (2 μM PACAP-3-desthiobiotin mixed with 20 μM Streptavidin). The injection cannula was then lowered, while applying positive pressure of 0.1 μL/min to avoid air bubbles, into the previously implanted cannula guide. Next, the Hamilton syringe was placed in a remote infuse/withdraw dual syringe pump (PHD 2000 Syringe Pump; Harvard Apparatus, Holliston, MA). Animals with their radiofrequency (surface and volume) coils (Doty Scientific, Columbia, SC) were inserted into the magnet bore and locked in a position such that the head of the animal was at the center of the magnet bore.

MRI and data analysis. Animals were scanned by MRI to measure the changes in hemodynamic contrast at the site of xenografted cells following distal sensor injection. High resolution T_2-weighted anatomical scans of each animal were obtained using a rapid acquisition with relaxation enhancement (RARE) pulse sequence with TE = 44 ms, TR = 2,500 ms, RARE factor 8, spatial resolution 100 μm x 100 μm x 1 mm, and matrix size 256 x 256 with seven slices. Hemodynamic contrast image series were acquired using a gradient echo planar imaging (EPI) pulse sequence with TE = 25 ms, TR = 2,000 ms, spatial resolution 390 μm x 390 μm x 1 mm, and matrix size 64 x 64 with seven slices. Ten minutes of baseline measurement with 4 s per time point were acquired before probe infusion. Following this baseline period, while continuously collecting EPI scans, infusion pump was remotely turned on to commence distal sensor injection (into the CSF) of 40 μl aliquot of 2 μM PACAP-3-desthiobiotin caged with 20 μM Streptavidin at a rate of 1 μl/min through the distal delivery cannula. EPI scans continued being collected for 10 minutes after the infusion of the sensor had stopped for a total scan time of 60 minutes. MRI data was processed and analyzed using the AFNI software. The AFNI 3dAllineate command was used to align each animal's EPI data set to the corresponding RARE anatomical

image. Each animal's image data were then aligned to the cell injection site of a reference anatomical MRI and normalized by assigning the mean of the baseline time period to 100 using AFNI's 3dcalc command. To identify voxels with signal changes characteristic of vasodilatory response, AFNI's 3dDeconvolve command using PACAP-specific signal time course was used as a stimulus and regressing against the motion parameters of each animal. For visualization, group beta coefficient maps, thresholded by the F statistic, were overlaid on a reference anatomical image. Representative animal signal change maps were overlaid on a reference anatomical image for comparison of the MRI cell localization data to the sensor localization fluorescence images. Time courses were obtained by averaging MRI signal over 2.5 x 2.5 mm regions of interest defined as the area of the cell implantation in individual animals' datasets and standard error was calculated across animals using MATLAB. The plateau percent signal change was determined by comparing signal values during baseline and after the infusion conditions.

Histology. After biotinylated and control cell implantation and distal sensor infusion as described above with the exception of replacing Streptavidin caging domain with Streptavidin-DyLight 488 to allow fluorescent visualization, animals were transcardially perfused with phosphate buffered saline followed by 4% paraformaldehyde in phosphate buffered saline. Brains were extracted, post-fixed overnight at 4 °C, and sectioned the following day. Free-floating sections (50 µm) were cut using a vibratome (Leica VT1200 S, Leica Microsystems Gmbh, Wetzlar, Germany), mounted on glass slides with Invitrogen ProLong Gold Antifade Mountant (Fisher Scientific Company, Ottawa, Ontario, Canada) and protected with a coverslip. The sensor diffusion into the area of the cell

implantation was visualized by green fluorescence due to the presence of DyLight 488 on the biotinylated cell side of the brain. The biotin on the cell surface outcompeted Streptavidin-DyLight 488 from PACAP-3-desthiobiotin and made it possible to visualize that the sensor does travel to the cell implantation site. The xenografted cells were visualized using DAPI staining (1:1000), followed by one wash with PBS + 0.5% BSA. The fluorescence imaging was performed using confocal microscopy (Axio Imager 2; Zeiss, Thornwood, NY).

References

1. Kim, S. A. & Jun, S. B. In-vivo Optical Measurement of Neural Activity in the Brain. *Exp. Neurobiol.* **22**, 158–166 (2013).
2. Yildirim, M., Sugihara, H., So, P. T. C. & Sur, M. Functional imaging of visual cortical layers and subplate in awake mice with optimized three-photon microscopy. *Nat. Commun.* **10**, 177 (2019).
3. Van de Bittner, G. C., Ricq, E. L. & Hooker, J. M. A philosophy for CNS radiotracer design. *Acc. Chem. Res.* **47**, 3127–3134 (2014).
4. Moses, W. W. Fundamental Limits of Spatial Resolution in PET. *Nucl. Instrum. Methods Phys. Res. Sect. Accel. Spectrometers Detect. Assoc. Equip.* **648 Supplement 1**, S236–S240 (2011).
5. Hillman, E. M. C. Coupling mechanism and significance of the BOLD signal: a status report. *Annu. Rev. Neurosci.* **37**, 161–181 (2014).
6. Deffieux, T., Demene, C., Pernot, M. & Tanter, M. Functional ultrasound neuroimaging: a review of the preclinical and clinical state of the art. *Curr. Opin. Neurobiol.* **50**, 128–135 (2018).
7. Su, Y. *et al.* Quantitative hemodynamic PET imaging using image-derived arterial input function and a PET/MR hybrid scanner. *J. Cereb. Blood Flow Metab.* **37**, 1435–1446 (2017).
8. Jennings, D., Raghunand, N. & Gillies, R. J. Imaging Hemodynamics. *Cancer Metastasis Rev.* **27**, 589–613 (2008).
9. Desai, M., Slusarczyk, A. L., Chapin, A., Barch, M. & Jasanoff, A. Molecular imaging with engineered physiology. *Nat. Commun.* **7**, 13607 (2016).
10. Robberecht, P. *et al.* Structural requirements for the occupancy of pituitary adenylate-cyclase-activating-peptide (PACAP) receptors and adenylate cyclase activation in human neuroblastoma NB-OK-1 cell membranes. *Eur. J. Biochem.* **207**, 239–246 (1992).
11. Hattori, S. *et al.* Comprehensive behavioral analysis of pituitary adenylate cyclase-activating polypeptide (PACAP) knockout mice. *Front. Behav. Neurosci.* **6**, (2012).

12. Green, N. M. Avidin. 3. The nature of the biotin-binding site. *Biochem. J.* **89**, 599–609 (1963).
13. Sun, C. *et al.* Solution structure and mutational analysis of pituitary adenylate cyclase-activating polypeptide binding to the extracellular domain of PAC1-RS. *Proc. Natl. Acad. Sci.* **104**, 7875–7880 (2007).
14. Hofmann, K., Titus, G., Montibeller, J. A. & Finn, F. M. Avidin binding of carboxyl-substituted biotin and analogues. *Biochemistry* **21**, 978–984 (1982).
15. Hirsch, J. D. *et al.* Easily reversible desthiobiotin binding to streptavidin, avidin, and other biotin-binding proteins: uses for protein labeling, detection, and isolation. *Anal. Biochem.* **308**, 343–357 (2002).
16. Bartelle, B. B. *et al.* Novel Genetic Approach for In Vivo Vascular Imaging in Mice. *Circ. Res.* **110**, 938–947 (2012).
17. Looger, L. L. *et al.* A genetically encoded fluorescent sensor for in vivo imaging of GABA. (2018). doi:10.1101/322578
18. De Lorimier, R. M. *et al.* Construction of a fluorescent biosensor family. *Protein Sci. Publ. Protein Soc.* **11**, 2655–2675 (2002).
19. Marvin, J. S., Schreiter, E. R., Echevarría, I. M. & Looger, L. L. A genetically encoded, high-signal-to-noise maltose sensor. *Proteins Struct. Funct. Bioinforma.* **79**, 3025–3036 (2011).
20. Marvin, J. S. *et al.* An optimized fluorescent probe for visualizing glutamate neurotransmission. *Nat. Methods* **10**, 162–170 (2013).
21. Okumoto, S. *et al.* Detection of glutamate release from neurons by genetically encoded surface-displayed FRET nanosensors. *Proc. Natl. Acad. Sci. U. S. A.* **102**, 8740–8745 (2005).
22. Brun, M. A. *et al.* A Semisynthetic Fluorescent Sensor Protein for Glutamate. *J. Am. Chem. Soc.* **134**, 7676–7678 (2012).
23. Brun, M. A. *et al.* Semisynthesis of Fluorescent Metabolite Sensors on Cell Surfaces. *J. Am. Chem. Soc.* **133**, 16235–16242 (2011).
24. Griss, R. *et al.* Bioluminescent sensor proteins for point-of-care therapeutic drug monitoring. *Nat. Chem. Biol.* **10**, 598–603 (2014).
25. Masharina, A., Reymond, L., Maurel, D., Umezawa, K. & Johnsson, K. A Fluorescent Sensor for GABA and Synthetic GABAB Receptor Ligands. *J. Am. Chem. Soc.* **134**, 19026–19034 (2012).
26. Schena, A. & Johnsson, K. Sensing Acetylcholine and Anticholinesterase Compounds. *Angew. Chem. Int. Ed.* **53**, 1302–1305 (2014).
27. Slusarczyk, A. L. (Adrian L. Molecular imaging with engineered physiology. (Massachusetts Institute of Technology, 2016).

Chapter 3: Largescale noninvasive delivery of nanoparticles to brain parenchyma

Introduction

The ever-expanding menu of molecular fMRI probes includes protein-based sensors, like the vasoprobes of Chapter 2, as well as many other interesting contrast agents, but to study and treat the brain, widespread delivery to the brain parenchyma is essential. One way to transport molecular probes to the brain is to transiently open the BBB. Numerous studies have shown that focused ultrasound-mediated BBB opening is successful in delivering various targets[1–6] to highly localized regions of the brain, hence effectively improving treatment of brain tumors[7]. However, focused ultrasound, resulting in very targeted delivery, is not suitable for treatment of diseases with unclear or scattered lesions in various areas of the brain, like Alzheimer's disease[8,9]. Likewise, widespread delivery of molecular sensors into the brain is highly desirable to probe the interplay of signaling molecules in the brain. The utility of unfocused ultrasound has been demonstrated in mice to detect amyloid plaques[9] and map neuronal activity with manganese[10].

Here, unfocused ultrasound-mediated BBB opening is applied to rats, which allows widespread delivery throughout a quarter of the rat brain. The efficacy of this delivery technique is tested on a model of the promising novel platforms for sensing calcium signaling in the brain based on superparamagnetic iron oxide nanoparticles (SPIONs)[11–13]. We previously proposed SPIONs as a potential alternative to gadolinium-based T_1 contrast agents[14] after Gd^{3+} release was linked to nephrogenic systemic fibrosis[15] – a rare

but devastating disorder. We further optimized the previously reported SPIONs by shrinking their core to 1 nanometer to facilitate SPIONs spreading through the brain parenchyma after opening the BBB[16].

Here we visualize widespread delivery of 1 nm SPIONs into brain parenchyma by T_1-weighted MRI imaging in live rodent brains and iron staining in histological analysis following widespread ultrasound-mediated BBB disruption. We further demonstrate that vasculature in sonicated brains remains intact, which validates this technique as a potential delivery vehicle for imaging agents that aspire to study large regions of the brain.

Results

Note: Synthesis and size determination of SPIONs were performed by Dr. He Wei, the imaging of histological slices was done in collaboration with Dr. Peter Harvey, and the iron staining was done in collaboration with Dr. He Wei.

Synthesis and size determination of 1 nm SPIONs

We minimized the size of SPIONs to just 1 nm core size by adjusting the solvent mixture and control of thermal decomposition temperature (Figure 3-1a). Since our nanoparticles are too small to be detectable using transmission electron microscopy, we quantified the hydrodynamic diameter (HD) of the resulting nanoparticles by size-exclusion column (Superose^{TM} 6) calibrated by protein standards[17,18] (Figure 3-1b). We indirectly determined the size of the iron oxide core after the ligand exchange from previous experience that the water soluble zwitterion-based ligand used to coat the iron oxide core

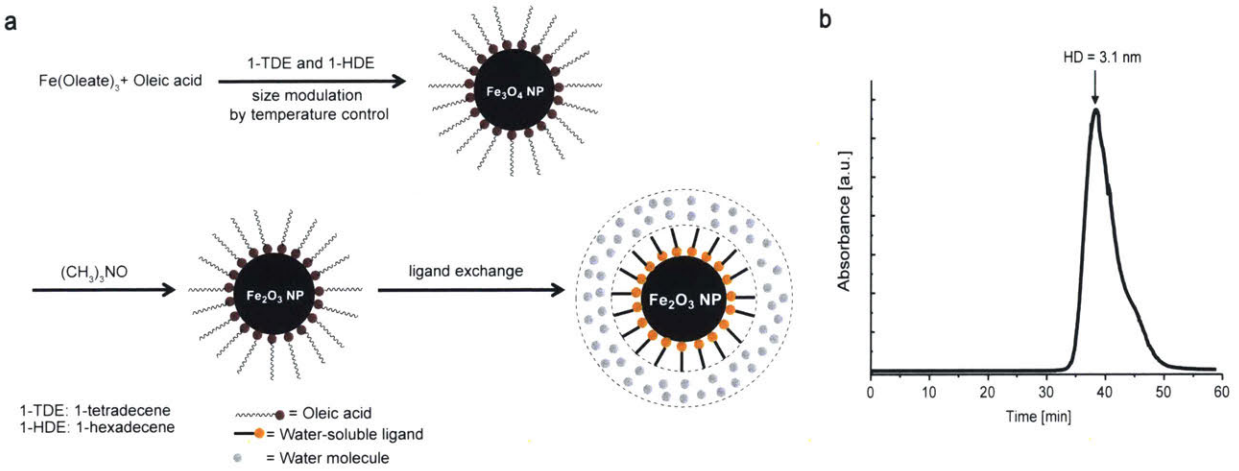

Figure 3-1. Characterization of 1 nm SPIONs: **a**: Synthesis steps of 1 nm SPIONs; **b**: Hydrodynamic diameter (HD) characterization by size-exclusion column as previously described in Wei et al 2012 and 2013[17,18].

always adds 2 nm to the total hydrodynamic diameter[14,19]. Since the HD is determined to be 3 nm, the nanoparticles' inorganic core must be 1 nm, resulting in small SPIONs that are well suited to effectively penetrate brain parenchyma.

MRI assessment of 1 nm SPIONs delivery to the brain by microbubble-enhanced ultrasound BBB opening

We applied ultrasound waves in combination with microbubbles circulating in vasculature to transiently open the BBB in rodent brains (Figure 3-2a). In this mode of BBB opening, the tight junctions, located in between the endothelial cells lining blood vessels in the brain, widen and allow analytes to diffuse into the brain. We successfully delivered 1 nm SPIONs into the brain via intravenous (I.V.) injection following ultrasound-mediated BBB-disruption. The T_1 contrast change due to SPIONs is visible by eye in raw MRI signal intensity change (Figure 3-2c) following intravenous administration of contrast compared

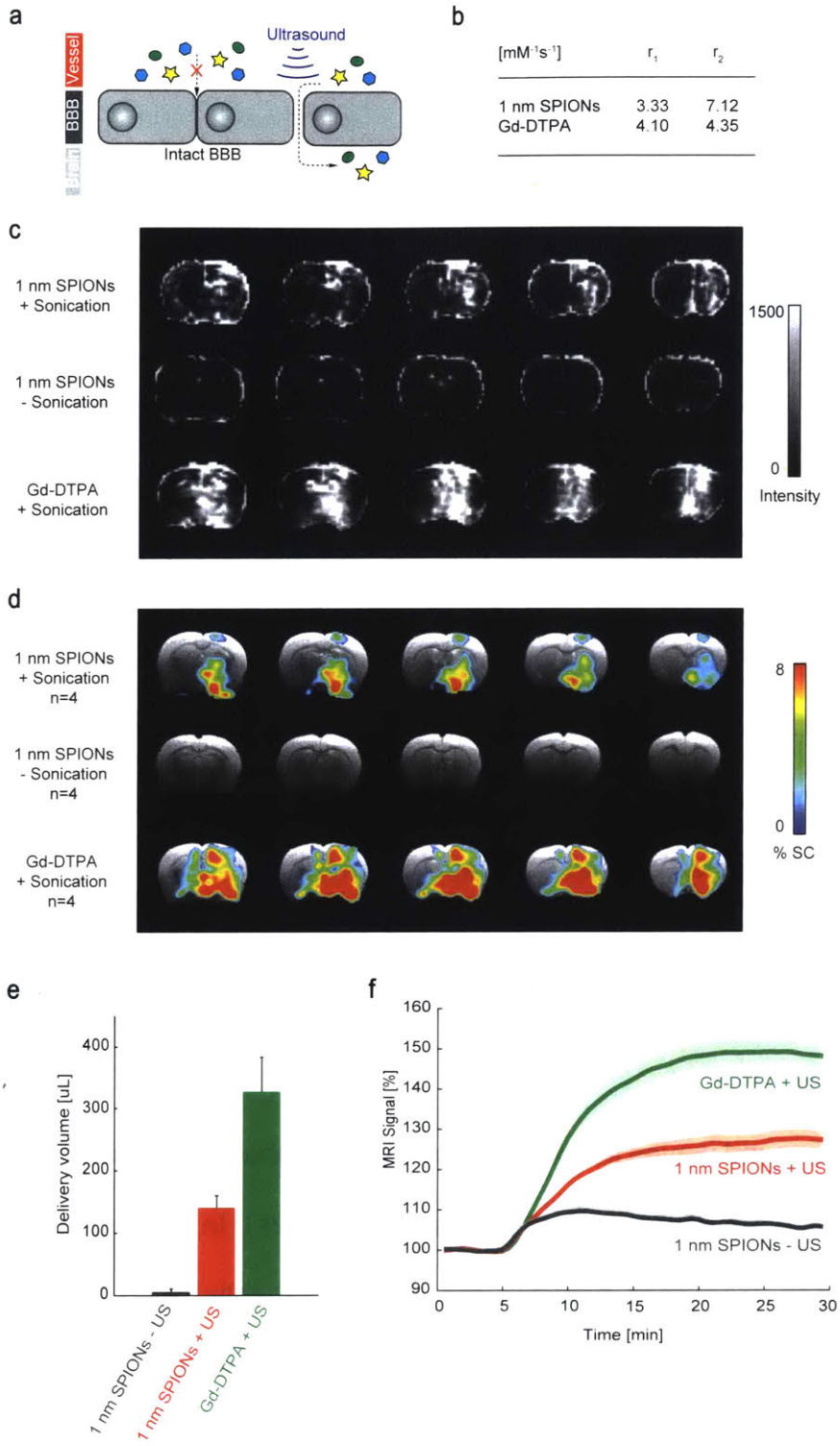

Figure 3-2. *In vivo* MRI assessment of SPIONs delivery to the brain: **a**: Schematic of ultrasound-mediated delivery across the BBB; **b**: Relaxivity measurements at 9.4 T comparing 1 nm SPIONs to Gd-DTPA; **c**: Raw MRI signal intensity change in a representative animal of each group after I.V. injection of 50 mM 1 nm SPIONs compared to 50 mM Gd-DTPA control, and no sonication condition. **d**: Group signal change (SC) maps overlayed on anatomical images visualizing areas with sustained MRI signal increase after I.V. injection of 1 nm SPIONs or Gd-DTPA control (n=4 for each condition). **e**: Quantification of the size of the delivery volume in the brain for each condition tested, standard error reported across animals. **f**: Time courses of MRI signal in region of interest with sustained delivery to the brain in sonicated (+US) vs. unsonicated (-US) brains after I.V. delivery of 1 nm SPIONs or Gd-DTPA control; I.V. injection occurs between 5-10 minutes on the time course.

to control unsonicated brains. We visualized and quantified the regions with sustained high T_1-weighted signal in MRI following I.V. contrast injection (Figure 3-2d-e) signifying regions of contrast agent delivery to the brain. The signal in areas less affected by sonication tends to decay following the initial spike by contrast injected into vasculature. Interestingly, with the same sonication and injection conditions, the spread of Gd-DTPA in the brain is broader and results in higher MRI signal compared to 1 nm SPIONs (Figure 3-2c-f). We hypothesize that the wider spread and the higher signal change for gadolinium occurs because there are more molecules of Gd-DTPA injected than total number of nanoparticles, since the 50 mM concentration is determined by iron content and each nanoparticle contains multiple iron oxides. Additionally, Gd-DTPA size is on the order of 1 nm, ~threefold smaller than 3 nm HD diameter of the SPIONs, likely allowing better spread and tissue permeability for the smaller agent. We also compared the relaxivities of 1 nm SPIONs and Gd-DTPA and found SPIONs longitudinal relaxivity to be slightly lower (r_1 = 3.33 $mM^{-1}s^{-1}$) compared to Gd-DTPA (r_1 = 4.10 $mM^{-1}s^{-1}$) (Figure 3-2b), which would result in moderately lower contrast enhancement *in vivo*.

Histological assessment of the spread of 1 nm SPIONs in the brain tissue and of the health of vasculature post-BBB opening

We assessed the SPION spread through the brain tissue by iron staining in histological slices. We found that the SPION deposits followed the shape of regions of sustained MRI signal increase following the I.V. contrast injection (Figure 3-3l.a). No iron deposits were found in unsonicated brain (Figure 3-3l.c) and only slight iron deposition was visualized at the bottom of the brain in most intense sonication area following Gd-DTPA I.V. injection

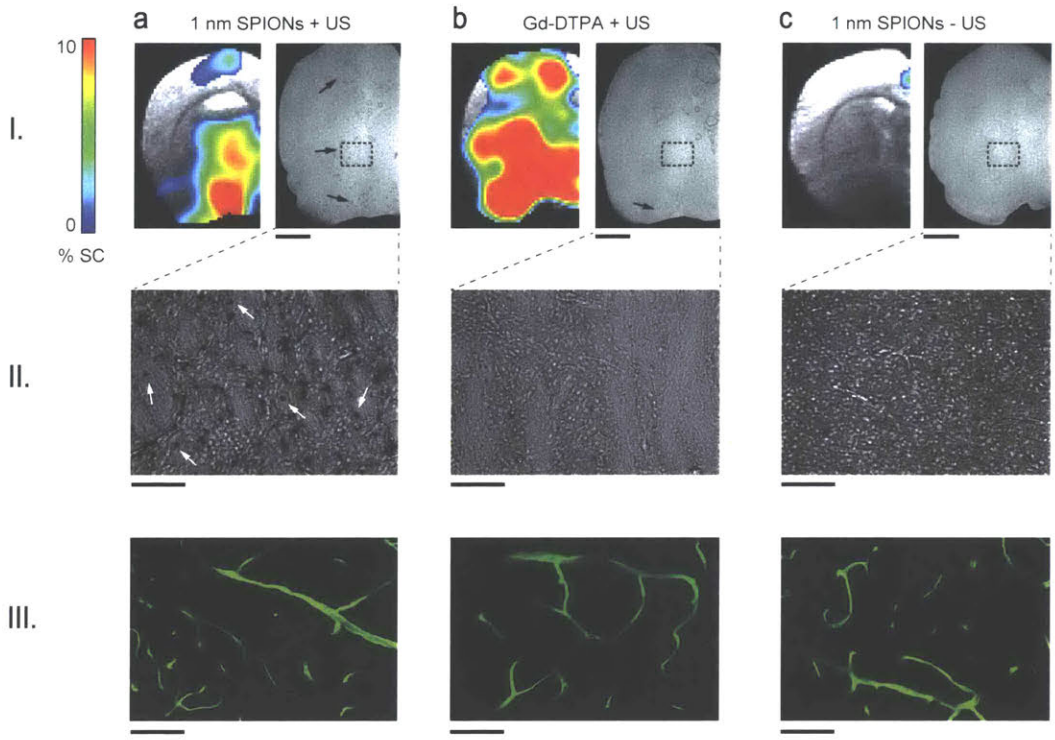

Figure 3-3. Histological assessment of the spread of SPIONs in the brain. The three columns indicate three delivery conditions, each at 50 mM **a**: 1 nm SPIONs after sonication (+US), **b**: Gd-DTPA after sonication, and **c**: 1 nm SPIONs without sonication (-US). The rows indicate different type of data illustrating SPION spread in brain parenchyma **I**: MRI signal change overlaid on anatomical image in histologically analyzed animals (left), and brightfield image of sonicated brain half following iron staining (right); the black arrows indicate stained iron-deposits; scale bar = 2 mm. **II**: 10x magnification of histological brain slices in brightfield, the white arrows indicate stained SPIONs that appear to have crossed into brain parenchyma; scale bar = 200 µm. **III**: tomato lectin – DyLight 488 staining of endothelial cells lining vasculature at 20x magnification; scale bar = 20 µm.

(Figure 3-3I.b). The iron deposits in the gadolinium control animal most likely come from extravasated red-blood cells, which is evidenced by their disappearance within 2 weeks after slice preparation, consistent with unstable heme groups. BBB opening efficiently delivers SPIONs into brain parenchyma (Figure 3-3II). There is no apparent difference in vasculature appearance for sonicated brains compared to control animals (Figure 3-3III), suggesting that the integrity of blood vessels in sonicated animals remains intact.

Discussion

We have demonstrated largescale delivery of nanoparticles into deep regions of brain parenchyma in living rodent brains following ultrasound-mediated BBB opening. Currently the delivery region covers around a quarter of the brain but the technique has potential to be expanded to cover the entire rat brain by applying multiple sonications over four quadrants of the brain. However, multiple sonication approach would need to be optimized to avoid potential overlap of sonicated brain regions, which could create areas in the brain where repeated sonication damaged vasculature, in turn complicating the ability to study mechanistic processes in these areas.

Ultrasound-mediated BBB opening could be applied to deliver various imaging agents across the BBB, thus potentially enabling mechanistic neuroimaging of the entire brain. Based on previous studies[6], we would expect the efficiency of delivery to be size-dependent: the larger the imaging agent, the less efficient its delivery and the stronger ultrasound parameters need to be applied for the agent to successfully get across the BBB. We have demonstrated some evidence towards the size dependence of the delivery as demonstrated by ~three times broader spread of ~1nm HD Gd-DTPA (quantified by sustained MRI signal increase in Figure 3-2d-e) compared to 3 nm HD SPIONs, which would suggest proportional dependence of the spread in brain parenchyma to the size of the delivered moiety. However, the results presented here are complicated because the concentration of nanoparticles was determined by iron content, resulting in fewer nanoparticles injected compared to the number of Gd-DTPA molecules because each nanoparticle is loaded with multiple iron oxides. A better comparison of the size-

dependence of the spread in the brain would match the Gd-DTPA concentration to the number of nanoparticle molecules per volume unit.

As a next step, we would apply the same sonication to attempt to deliver slightly larger moieties that could study molecular signaling events in the brain, e.g. 6 nm HD SPIONs functionalized for calcium detection, which are currently in development in our group. Another promising imaging agents that could benefit from ultrasound-mediated delivery are the vasoprobes discussed in Chapter 2. The vasoprobe sensors are on the order of 5 nm HD, making them similar in size to the smallest existing functionalized SPIONs and potentially small enough for widespread delivery throughout the brain using ultrasound. Furthermore, the demonstrated health of vasculature following ultrasound-mediated BBB opening suggests that vascular readouts afforded by theses sensors could be fully functional following the sonication. If ultrasound-mediated delivery of vasoprobe sensors would be successful, these probes would enable unprecedented ability to sense small molecule targets at nanomolar concentrations throughout large regions in the brain.

Methods

Synthesis and size-characterization of 1nm SPIONs. These methods were performed as previously described in Dr. He Wei's thesis[19].

Relaxivity characterization of 1nm SPIONs using 9.4 T MRI. MRI data were acquired on a 9.4 T Bruker Biospec system. Longitudinal and transverse relaxivity (r_1 and r_2) measurements were acquired using a 2D spin echo sequence (echo time (TE) = 10,

20, 30, 40, and 50 ms, repetition time (TR) = 100, 200, 300, 400, and 500 ms). r_1 and r_2 values were generated using MATLAB scripts (Mathworks, Natick, MA) written in house.

Animal procedures. All animal procedures were conducted in accordance with National Institutes of Health guidelines and with the approval of the MIT Committee on Animal Care. All experiments were performed with male Sprague-Dawley rats, age 5–6 weeks, supplied by Charles River Laboratories (Wilmington, MA).

Magnetic Resonance Imaging. Twelve Sprague-Dawley rats were used for *in vivo* MRI experiments. Data were acquired on a 9.4 T 20 cm inner diameter, horizontal bore magnet (Bruker BioSpec MRI, Ettlingen, Germany) with the surface and volume radiofrequency coil setup (Bruker, Billerica, MA) positioned as described in the following sections.

Semi-permanent tail vein catheter placement. Twelve aneasthesized rats underwent the placement of the tail vein catheter for microbubble injection for BBB disruption and contrast delivery in the MRI scanner. The tail vein was visualized by application of alcohol to the skin of the tail. A catheter (24 GA Surflo, Terumo, Somerset, NJ) was slowly inserted into the tail vein until obvious blood back-flow was achieved. The catheter was secured to the tail by placing a tongue depressor (Puritan, Guilford, ME) underneath the tail and taping the tail and the tongue depressor together using surgical tape. The catheter was flushed with 0.5% heparin in PBS to prevent clotting and secured with a stopper until the contrast infusion in the MRI.

Ultrasound-mediated disruption of the BBB. Eight rats underwent the procedure to disrupt their BBB using ultrasound. The rats were induced using 3% isoflurane (ISO) anesthesia and maintained using 2% ISO with vacuum suction turned on to remove excess anesthetic. The rats' eyes were covered with paralube vet ointment (Dechra Veterinary Products, Overland Park, KS) to prevent eyes from drying from exposure to ISO. The rats' heads were shaved and cleaned with alcohol and povidone-iodine prep pads for easy access to the skull. Using sterile surgical equipment, the skin over the skull was retracted and the skull cleared of tissue so that coronal and sagittal sutures on the skull were clearly visible. The sonication equipment was assembled by attaching the custom-made transducer (XDR060B S/N 008 500 kHz x 25 mm Planar Transducer, Sonic Concepts, Bothwell, WA) to its housing holder filled with slowly circulating de-ionized water (degassed overnight). The sound waves were generated by function generator (25MHz Arbitrary Waveform/Function Generator, BK Precision, Yorba Linda, CA) with the following settings: 500 kHz driving frequency, 0.2 V amplitude, 5,000 burst count, and 1 s burst rate. The signal was amplified by power amplifier (ENI Model 550L RF Power Amplifier 50 Watts Linear, Bell Electronics, Renton, WA), went through impedance matching network (Fundamental Resonance Impedance Matching Network, Sonic Concepts, Bothwell, WA) and, finally, to the transducer. The transducer housing assembly center was positioned 1mm above the skull, 2 mm from the midline and 3 mm posterior to bregma, and was coupled with ultrasound transmission gel (Parker Aquasonic, Fairfield, NJ) to the skull to avoid air interface. The sonication was started by turning on the signal from the function generator and lasted 5 minutes. Immediately after the

sonication was turned on, 50 μL of microbubbles (Optison Perflutren Protein-Type A Microspheres Injectable Suspension, GE Healthcare, Chicago, IL) were injected through the tail vein catheter and flushed with 0.2 mL of 0.5% heparin in PBS. The sonication happened within 10 – 20 minutes after the degassed water was taken off from vacuum. After the sonication was completed, the skin was glued together using tissue glue and the animal was immediately transferred to the MRI scanner for imaging.

MRI assessment of the delivery of contrast agent.

Experimental setup. Immediately after the surgical preparation, twelve rats (8 having undergone sonication + 4 unsonicated control animals, all with tail vein catheter in place) were imaged during T_1 contrast I.V. infusion. For the imaging experiments, animals were anesthetized using 2% ISO in oxygen-enhanced air. The animals were fixed by ear bars into a custom built cradle for imaging with a commercial surface radiofrequency phase array (Bruker, Billerica, MA) fitting snugly around the head. Heart rate and spO_2 were continuously monitored. Immediately before each experiment, the I.V. tail vein injection catheter was attached via non-sticky tubing (PTFE 0.7 mm id 1.6 mm od, Agilent Technologies, Santa Clara, CA) to a 10 mL plastic syringe that was prefilled with the appropriate I.V. injection solution (50 mM of 1 nm SPIONs or 50 mM of Gd-DTPA). Next, the syringe was placed in a remote infuse/withdraw dual syringe pump (PHD 2000 Syringe Pump; Harvard Apparatus, Holliston, MA). Animals within the radiofrequency (surface and volume) coil setup (Bruker, Billerica, MA) were inserted into the magnet bore and locked in a position such that the head of the animal was at the center of the magnet bore.

MRI acquisition. Animals were scanned by MRI to measure the changes in T_1 contrast following I.V. injections. High resolution T_2-weighted anatomical scans of each animal were obtained using a rapid acquisition with relaxation enhancement (RARE) pulse sequence with TE = 56 ms, TR = 5,000 ms, RARE factor 8, spatial resolution 156 μm x 156 μm x 1 mm, and matrix size 128 x 128 with six slices. T_1-weighted contrast time series were acquired using a RARE pulse sequence with TE = 8.45 ms, TR = 680 ms, spatial resolution 400 μm x 400 μm x 1 mm, and matrix size 50 x 50 with six slices. Five minutes of baseline measurement with 30 s per time point were acquired before contrast infusion. Following this baseline period, while continuously collecting RARE T_1-weighted scans, the infusion pump was remotely turned on to commence I.V. injection of 1 mL of either 50 mM 1 nm SPIONs or 50 mM Gd-DTPA solutions at a rate of 0.2 mL/min through the tail vein catheter. RARE scans continued being collected for 20 minutes after the infusion of the T_1 contrast agent had stopped for a total scan time of 30 minutes. This contrast injection process happened 45 – 60 minutes after sonication.

MRI data analysis. MRI data was processed and analyzed using the AFNI software. The AFNI 3dAllineate command was used to align each animal's dataset to the reference anatomical image. Each animal's data was normalized by assigning the mean of the baseline time period to 100% using AFNI's 3dcalc command. To identify voxels with significant delivery to the brain according to T_1-weighted signal, the signal 20 minutes after the contrast injection was compared to the signal immediately after the contrast infusion in the group concatenated data. This change is indicative of delivery as the contrast in the blood vessels would decrease after the infusion has stopped through renal clearance, whereas the signal in brain parenchyma with contrast present would continue

to increase as more contrast is accumulated there over time. The regions of contrast delivery were characterized as voxels with signal change increase, after the contrast injection has stopped, of 1.5% or greater. For visualization, group signal change maps were overlaid on a reference anatomical image. The time courses were obtained from sphere regions of interest with 0.8 mm radius defined around peak signal change areas in the group dataset; the standard error was calculated across animals using MATLAB.

Histology. Following MRI, animals were transcardially perfused with phosphate buffered saline containing 2 mg/kg tomato lectin labeled with DyLight 488 (Vector Laboratories, Burlingame, CA) followed by 4% paraformaldehyde in phosphate buffered saline. Brains were extracted, post-fixed overnight at 4 °C, and sectioned within a week. Free-floating sections (50 μm) were cut using a vibratome (Leica VT1200 S, Leica Microsystems Gmbh, Wetzlar, Germany), mounted on glass slides with Invitrogen ProLong Gold Antifade Mountant (Fisher Scientific Company, Ottawa, Ontario, Canada), and protected with a coverslip. The health of vasculature in sonicated brains was visualized by DyLight 488 on tomato lectin, which binds to the vascular endothelial cells. The fluorescence imaging was performed using confocal microscopy (Axio Imager 2; Zeiss, Thornwood, NY).

Iron quantification in brain slices by Prussian Blue staining. Previously extracted (as described above) 50 μm brain slices were submerged in 0.5 mL of iron stain (1:1 mixture of potassium ferrocyanide and hydrochloric acid, Abcam, Cambridge, MA) for 30 minutes. The slices were then rinsed 4 times with 0.5 mL of distilled water, dehydrated in 0.5 mL

of 95% alcohol followed by 0.5 mL of absolute alcohol. The slices were then mounted on glass slides with Invitrogen ProLong Gold Antifade Mountant (Fisher Scientific Company, Ottawa, Ontario, Canada) and protected with a coverslip. The slides were imaged in brightfield microscope at 1.25x and 10x magnifications.

References

1. Fan, C.-H. *et al.* Drug-loaded bubbles with matched focused ultrasound excitation for concurrent blood-brain barrier opening and brain-tumor drug delivery. *Acta Biomater.* **15**, 89–101 (2015).
2. Liu, H.-L. *et al.* Focused Ultrasound Enhances Central Nervous System Delivery of Bevacizumab for Malignant Glioma Treatment. *Radiology* **281**, 99–108 (2016).
3. Fan, C.-H. *et al.* Ultrasound/Magnetic Targeting with SPIO-DOX-Microbubble Complex for Image-Guided Drug Delivery in Brain Tumors. *Theranostics* **6**, 1542–1556 (2016).
4. Samiotaki, G., Acosta, C., Wang, S. & Konofagou, E. E. Enhanced delivery and bioactivity of the neurturin neurotrophic factor through focused ultrasound-mediated blood--brain barrier opening in vivo. *J. Cereb. Blood Flow Metab. Off. J. Int. Soc. Cereb. Blood Flow Metab.* **35**, 611–622 (2015).
5. Alkins, R., Burgess, A., Kerbel, R., Wels, W. S. & Hynynen, K. Early treatment of HER2-amplified brain tumors with targeted NK-92 cells and focused ultrasound improves survival. *Neuro-Oncol.* **18**, 974–981 (2016).
6. Choi, J. J., Wang, S., Tung, Y.-S., Morrison, B. & Konofagou, E. E. Molecules of various pharmacologically-relevant sizes can cross the ultrasound-induced blood-brain barrier opening in vivo. *Ultrasound Med. Biol.* **36**, 58–67 (2010).
7. Poon, C., McMahon, D. & Hynynen, K. Noninvasive and targeted delivery of therapeutics to the brain using focused ultrasound. *Neuropharmacology* **120**, 20–37 (2017).
8. Zhao, B. *et al.* Blood-brain barrier disruption induced by diagnostic ultrasound combined with microbubbles in mice. *Oncotarget* **9**, 4897 (2018).
9. Santin, M. D., Debeir, T., Bridal, S. L., Rooney, T. & Dhenain, M. Fast in vivo imaging of amyloid plaques using μ-MRI Gd-staining combined with ultrasound-induced blood-brain barrier opening. *NeuroImage* **79**, 288–294 (2013).
10. Howles, G. P., Qi, Y. & Johnson, G. A. Ultrasonic disruption of the blood-brain barrier enables in vivo functional mapping of the mouse barrel field cortex with manganese-enhanced MRI. *NeuroImage* **50**, 1464–1471 (2010).
11. Atanasijevic, T., Shusteff, M., Fam, P. & Jasanoff, A. Calcium-sensitive MRI contrast agents based on superparamagnetic iron oxide nanoparticles and calmodulin. *Proc. Natl. Acad. Sci.* **103**, 14707–14712 (2006).

12. Okada, S. *et al.* Calcium-dependent molecular fMRI using a magnetic nanosensor. *Nat. Nanotechnol.* **13**, 473 (2018).
13. Rodriguez, E., Lelyveld, V. S., Atanasijevic, T., Okada, S. & Jasanoff, A. Magnetic nanosensors optimized for rapid and reversible self-assembly. *Chem. Commun.* **50**, 3595–3598 (2014).
14. Wei, H. *et al.* Exceedingly small iron oxide nanoparticles as positive MRI contrast agents. *Proc. Natl. Acad. Sci.* 201620145 (2017). doi:10.1073/pnas.1620145114
15. Bennett, C. L. *et al.* Gadolinium-induced nephrogenic systemic fibrosis: the rise and fall of an iatrogenic disease. *Clin. Kidney J.* **5**, 82–88 (2012).
16. Mullin, L. B., Phillips, L. C. & Dayton, P. A. Nanoparticle Delivery Enhancement With Acoustically Activated Microbubbles. *IEEE Trans. Ultrason. Ferroelectr. Freq. Control* **60**, (2013).
17. Wei, H. *et al.* Compact zwitterion-coated iron oxide nanoparticles for biological applications. *Nano Lett.* **12**, 22–25 (2012).
18. Wei, H., Bruns, O. T., Chen, O. & Bawendi, M. G. Compact zwitterion-coated iron oxide nanoparticles for in vitro and in vivo imaging. *Integr. Biol.* **5**, 108–114 (2013).
19. Wei, H. Synthesis and development of hydrophilic iron oxide nanoparticles for biomedical applications. (Massachusetts Institute of Technology, 2014).

Chapter 4: Towards a magnetic resonance-based readout of crossing the intact blood-brain barrier by antibody-based therapeutics targeted to the brain

Introduction

The ability to readily detect drug delivery to the brain across the blood-brain barrier (BBB) would accelerate and simplify the development of brain-targeted therapeutics. The blood-brain barrier poses an obstacle in reaching the brain by pharmaceuticals injected through the bloodstream[1,2]. Large molecules cannot pass across the BBB, which impairs the delivery of most therapeutic constructs targeted to the brain. Previous studies have shown that it is possible to hijack the natural transport mechanisms to the brain i.e. receptor-mediated transcytosis, in which the drug constructs are engineered to bind the receptors on the luminal side of vascular endothelium and, upon binding, the constructs are transported across the endothelial cells into the brain parenchyma proper[3]. However, extensive fine-tuning is required to ensure that the constructs get released on the brain side of the endothelium[4]. Instead of being released, the constructs can be degraded in the cell during the transport process, or the constructs might be transported to the brain side of the cell but, being bound too tightly, they might not be released once in the brain, precluding their pharmacologic function. The existing methods of accessing BBB crossing cannot distinguish between the constructs that reached the brain tissue and the ones stuck in endothelium. As a result, the expected pharmaceutical action is used as a readout of both the drug activity and the BBB crossing. The lengthy time of such a readout – the

pharmaceutical effect can take weeks to manifest – and the convolution of drug activity and BBB crossing make troubleshooting and optimization cumbersome.

Here, we summarize our initial efforts to develop a fast non-invasive way of accessing whether the constructs got into the brain, which, if eventually successful, would accelerate pre-clinical and clinical drug development for brain disorders such as Alzheimer's disease.

We used a new MRI imaging strategy recently developed in our laboratory, to detect BBB crossing. In this fundamentally novel technique, we artificially perturb blood flow by administering a vasoactive probe. The abundant magnetic contrast afforded by blood thus serves to amplify the detected molecular signal, allowing 1,000-fold lower quantities of probes to be used, compared to conventional MRI contrast agents. This method is especially suitable for detecting BBB crossing because the receptors for our vasoactive probes are on the brain side of the vascular endothelium requiring the probes to be released from the endothelium into the brain for vasodilation to occur.

In this chapter, we (1) establish the utility of a vasoactive probe called Maxadilan, which is reported to be more stable in the bloodstream compared to PACAP[5] used as the basis of vasoprobes discussed in Chapter 2, as an MRI-based readout of delivery to the brain parenchyma; (2) report the initial MRI signal effects after I.V. injections of the BBB-crossing antibody tagged with Maxadilan; and (3) discuss the caveat we have discovered that I.V. administration of a vasoactive peptides causes cardiovascular response manifesting as global heart rate increase. Further, we discuss troubleshooting steps necessary to take this work forward.

Results

Note: The *in vitro* characterization and expression of all discussed variants of Maxadilan were performed by Dr. Adrian Slusarczyk and previously reported in his thesis[6].

Maxadilan-based hemodynamic imaging

Our probe design is based on a vasoactive peptide called Maxadilan (Figure 4-1a), which comes from sandflies and causes vasodilation in mammalian skin by activating the PAC1 receptor with sub-nanomolar potency. The PAC1 receptor is an endogenous target of PACAP, which allowed us to use the CHO cell luminescence bioassay of Chapter 2 as a readout of PAC1 receptor activation by Maxadilan and its derivatives *in vitro*. For initial testing of Maxadilan vasodilatory activity, we fused the N-terminus of Maxadilan to the C-terminus of GFP via a previously reported linker[7] (Figure 4-1b). The attachment of Maxadilan to GFP mimicked the necessity to eventually attach the vasoprobe to a BBB-crossing antibody and allowed us to ascertain that Maxadilan still retains sub-nanomolar potency (Figure 4-1c-d). This result allowed the project to move forward as the delivery of nanomolar concentrations is achievable using trojan-horse antibodies[8].

Its high potency, even when attached to a large protein domain, makes Maxadilan attractive as a potential platform to detect BBB-crossing entities. Before proceeding further with engineering of Maxadilan and attaching it to a BBB-crossing antibody we first validated Maxadilan-dependent imaging contrast in the living rat brains (Figure 4-1e). Intracranial delivery of GFP-Maxadilan caused an easily detectable hemodynamic signal of 4.7 ± 0.8% in T_2*-weighted MRI compared to 2.4 ± 0.5% in response to control injections of artificial cerebrospinal fluid (aCSF) vehicle (Figure 4-1f).

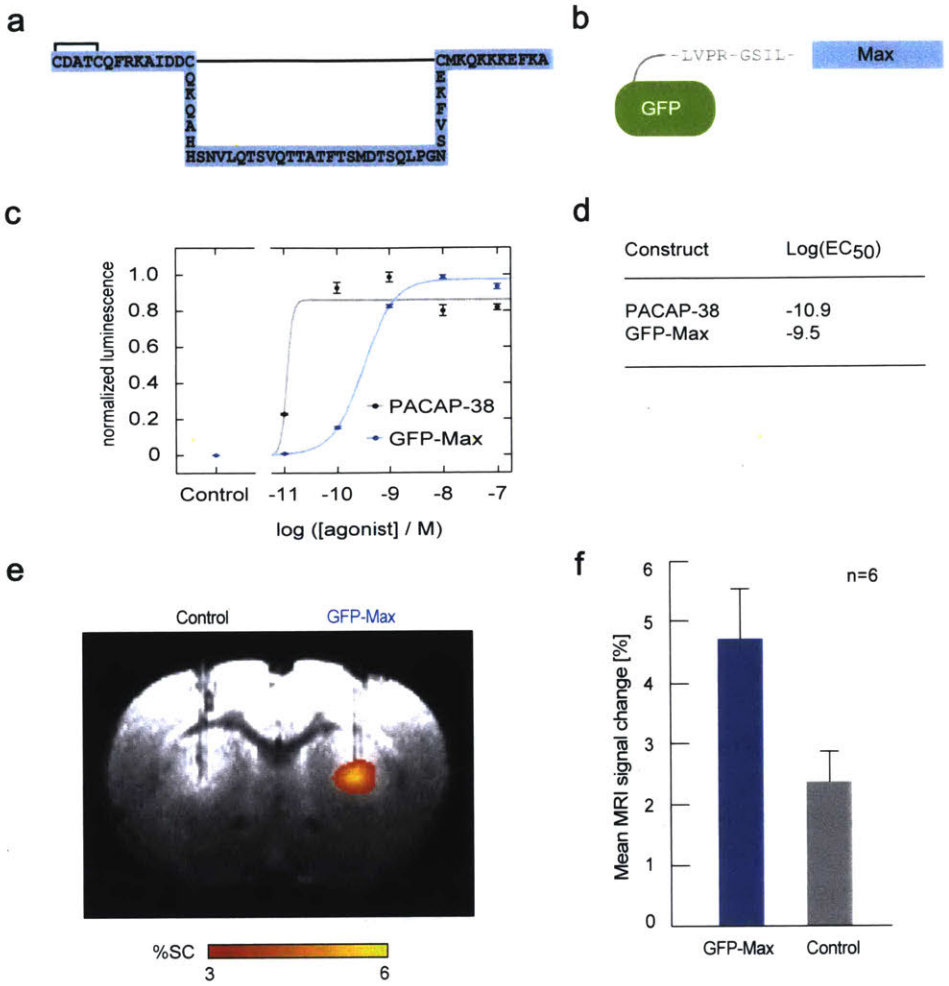

Figure 4-1. Maxadilan-based hemodynamic imaging: **a**: Sequence of Maxadilan vasoactive peptide with disulfide bonds shown as lines; **b**: The probe form used for in vitro characterization and in vivo testing: N-terminus of Maxadilan was attached to the C-terminus of GFP to resemble attachment to a large BBB-crossing antibody and ensure sufficient vasodilatory activity in this configuration. **c**: Comparison of PACAP and GFP-Maxadilan activities assessed by CHO cell-based bioassay for PAC1 receptor activation. **d**: potency values for PACAP and GFP-Maxadilan showing that nanomolar concentrations of GFP-Maxadilan are sufficient to cause receptor activation. **e**: In vivo MRI hemodynamic signal change due to intracranial injection of 100 nM GFP-Maxadilan vs control, signal change map was overlayed on the anatomical scan, n=6; **f**: Mean MRI signal change from a region underneath the cannula tip for the GFP-Maxadilan injection vs control with reported standard error.
Note: Panels a-d were adapted from the doctoral thesis by Dr. Adrian Slusarczyk with author's permission[6].

Active BBB-crossing construct design and in vivo testing

After validating the Maxadilan vasoprobe as a viable source for hemodynamic imaging with attachment of a large blocking domain, we next designed the BBB-crossing construct leveraging Maxadilan. We used the process of receptor-mediated transcytosis[9] as a basis

for transport to the brain (Figure 4-2a). In this process, the shuttle antibody binds to its receptor on vascular endothelial cells, gets recognized as an entity to be transported across the BBB, transported across the endothelial cell in a vesicle and released on the brain parenchyma side of the BBB, thus being delivered across. Further, we chose to work with a shuttle antibody called FC5[10,11], a robust and well-studied antibody fragment that is known to cross BBB[8,12,13]. We designed our probe to have FC5 on the transcytosis arm of the antibody and our vasoprobe attached as cargo (Figure 4-2b). Next, we showed that the BBB-crossing vasoprobe (FC5-Maxadilan fusion) still activates its PAC1 receptor at subnanomolar concentrations (Figure 4-2c).

We observed robust MRI signal increase following I.V. administration of the BBB-crossing vasoprobe compared to the control injection (Figure 4-2d-e). The steep dynamics of the response, its wide spread throughout the brain, and the signal decrease after the injection (Figure 4-2d) surprised us because FC5 is reported to accumulate in the brain over hours. These findings made us question whether vasoprobes injected I.V. produce systemic cardiovascular responses that affect the brain MRI signals. The BBB-crossing vasoprobe would only be effective as a readout of BBB crossing if its activity was dependent upon BBB-crossing and reaching PAC1 receptors on vascular smooth muscle cells on the brain side of the BBB (Figure 4-2a).

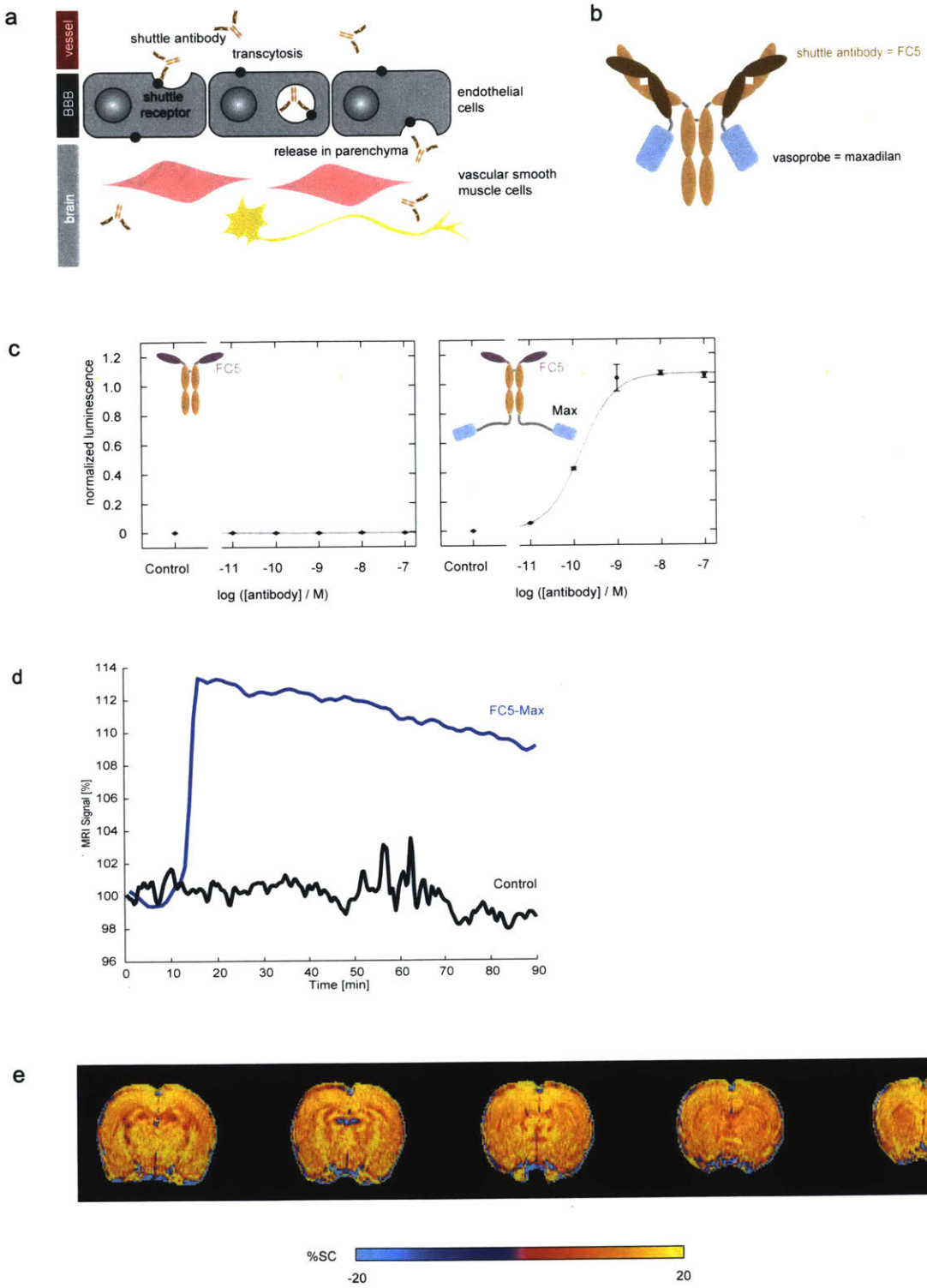

Figure 4-2. BBB-crossing construct design and *in vivo* testing: **a**: Schematic of the receptor-mediated transcytosis, which we leverage in our probe design; **b**: BBB-crossing construct design: shuttle antibody (FC5) is fused to Maxadilan vasoactive peptide. **c**: Comparison of FC5 BBB-crossing construct with and without Maxadilan in CHO cell-based bioassay for PAC1 receptor activation. **d**: Brain-wide MRI signal following I.V. injection of FC5-Maxadilan 6 mg/kg construct vs control. **e**: *In vivo* MRI hemodynamic signal change due to I.V. administration of FC5-Maxadilan overlayed on the anatomical scan.
Note: Panels a-c were adapted from the doctoral thesis by Dr. Adrian Slusarczyk with author's permission[6].

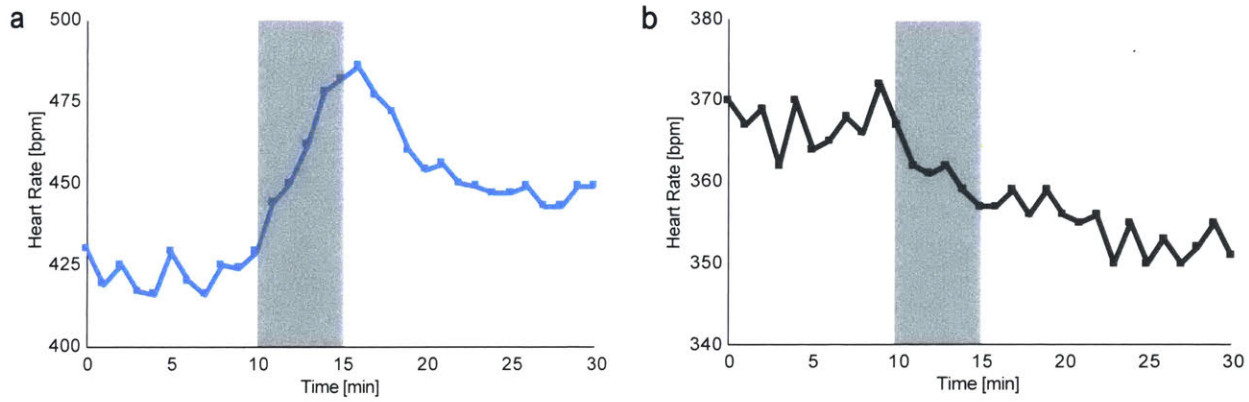

Figure 4-3. Vasoprobe I.V. injection effect on heart rate: **a**: Heart rate increase following I.V. injection of 1 ml of 2 μM vasoprobe; **b**: Heart rate change following I.V. injection of control. Gray bars indicate the duration of I.V. injection.

To examine the possibility of systemic vasoprobe effects, we monitored heart rate after vasoprobe I.V. injections compared to control injections and saw robust (>10%) heart rate increase even at small (2 μM) doses of vasoprobes (Figure 4-3a-b). Increasing doses of vasoprobes and lighter anesthesia magnified increase in heart rate following the I.V. injection (data not shown). Such an increase in heart rate could explain the increase in brain MRI signal following the I.V. injection of a BBB-permeable vasoprobe, regardless of its ability to penetrate the BBB.

Discussion

We have established Maxadilan vasoprobe as a promising platform for development of BBB-crossing constructs. Maxadilan tolerates attachments of protein fusion domains (we tested GFP and an FC5-based shuttle antibody) well and retains its vasodilatory ability both *in vitro* and in rodent brains. However, we discovered a global cardiovascular effect upon I.V. injection of BBB-crossing constructs. In order to function as an assay to detect BBB crossing, vasoprobe-shuttle antibody fusion must cause vasodilation only upon

crossing the endothelial cells forming the BBB. Currently, the injected construct is able to penetrate into tissue in all organs that do not possess the BBB. Hence, the vasoprobe is able to activate PAC1 receptors in virtually the entire organism (excluding the brain), triggering global cardiovascular response, detectable by profound heart rate increase upon injection of vasoprobes I.V.

The global cardiovascular effect we observed must be inhibited in order for vasoprobes to be considered as a potential basis for detection of BBB crossing. To remove these global effects, we would aim to prevent the vasoprobe from activating its receptor (PAC1 for Maxadilan) in the entire organism (except the brain). We could achieve this by I.V. injection of the receptor inhibitor that does not cross the BBB (e.g. PACAP(6-38)[14]). We could either co-inject the inhibitor with the BBB-crossing construct, or inject the inhibitor beforehand followed by vasoprobe construct injection after the dilatory activity elsewhere has been prevented. The timing of this process would need to be optimized.

Another avenue would be to characterize the systemic cardiovascular response well, across many animals, such that we could confidently correct MRI signal for any global effects. To this end, we could inject varying concentrations of a vasoprobe-antibody construct that does not cross the BBB, the construct should be as similar to the BBB-crossing construct as possible to give an identical global effect. We could then average the brain signal across many animals for each vasoprobe concentration and subtract (or regress) this signal from the response received due to BBB-crossing construct, hence hopefully isolating a brain-specific dilatory effect. Care should be taken to keep these

experiments as similar as possible (same anesthesia, animal age, length of surgical prep, MRI scanning method, vasoactive construct concentration).

Another possibility would be to wait until the global cardiovascular effect dissipates. This effect could be monitored using heart rate indication and establishing how long it takes for the heart rate to return to baseline following the injection of the vasodilatory probe. Our experiments indicate that the heart rate stabilizes ~10 minutes following the I.V. injection of vasoprobes at single digit micromolar concentrations (Figure 4-3a), however, the heart rate stabilizes at an increased level by ~6% compared to the heart rate prior to vasoprobe injection. After the duration of the global effect has been established, we could compare the MRI signal over time in animals that received BBB-crossing construct injection vs control animals and we would expect the brains with successfully delivered vasoprobe constructs to have an increasing trend due to vasoprobes activating their receptors on vascular smooth muscle cells past the BBB. We would expect fresh BBB-crossing constructs to be transported across the BBB over a long time as the antibodies are known to be stable in the bloodstream for days[15].

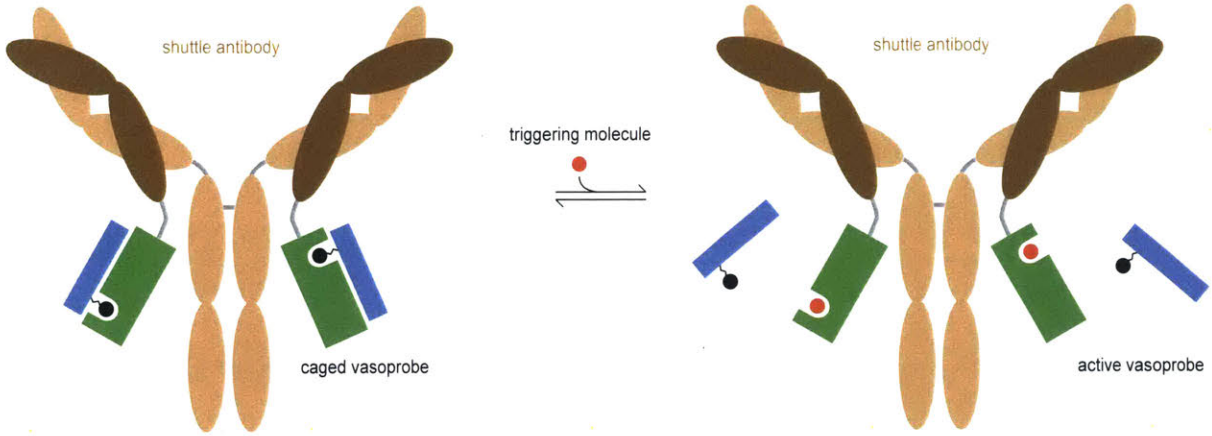

Figure 4-4. Concept of triggering dilation once the BBB-crossing construct gets transported into the brain: deliver caged vasoprobe on a shuttle antibody I.V., wait for any global vasodilatory signal to dissipate, trigger the vasodilatory readout by injecting a triggering BBB-penetrating molecule I.V., and observe hemodynamic signal in areas where the BBB-crossing construct got delivered to the brain.

A further strategy for creating specific readouts of BBB crossing would be to trigger the readout of BBB crossing after the BBB-crossing construct has accumulated in the brain (Figure 4-4). To this end, we would merge the shuttle antibody with the caged design of the small molecule sensor described in Chapter 2 (Figure 2-1b); the shuttle antibody could be fused to streptavidin, which in turn binds desthiobiotin attached to vasoprobe. For the readout of BBB crossing, we would first inject the BBB-crossing construct I.V., allow time for its accumulation in the brain and for any global cardiovascular signals to dissipate. Next, we would trigger the readout of BBB-crossing by pulsing the system with biotin delivered I.V. since biotin is a class B vitamin and is naturally transported to the brain[16]. Biotin would outcompete vasoprobes from their binding sites on streptavidin, freeing vasoprobes to bind their receptors and triggering hemodynamic readout in all brain regions where BBB-crossing construct got delivered.

There are two additional areas of study that could help us understand and improve candidate vasoprobe-mediated readouts of BBB-crossing: (1) mapping the vasoactive

probe receptor expression levels throughout the brain and understanding what signal change we could expect in different areas of the brain as a readout of delivery; and (2) characterizing the effectiveness of BBB-crossing of our constructs by staining for vasculature and injected BBB-crossing constructs.

Knowing what the positive readout of the delivery to the brain looks like throughout the entire brain is crucial for applying this method as a readout of delivery of any additional cargo. We do not expect the MRI signal change throughout the brain to be equal because the receptors of the vasoactive probes vary in distribution in different brain regions[17]. We would expect the signal increase to be larger in areas with bigger receptor expression levels, and smaller in regions with fewer receptors. The signal change variability could be studied by delivering BBB-crossing vasoactive constructs across many animals and averaging the MRI signal response, hence creating a map of "normal" readout of BBB-crossing. These results would be dependent on showing delivery across the brain by other common methods such as immunohistochemistry, as discussed in the next paragraph. Another way to characterize the signal change variability due to varying levels of vasoprobe receptors throughout the brain would be to inject the BBB-crossing vasoprobe construct intracranially into regions of different receptor expression levels. This approach would allow us to access the expected magnitude of signal change in different areas of the brain, independent of solving the global cardiovascular effect issue.

Another essential, and perhaps obvious, test is to check whether the BBB-crossing vasoactive constructs cross the BBB. To this end, we would fuse the BBB-crossing constructs to a fluorescent tag, extract the brains at different times following the tagged BBB-crossing construct I.V. injections, and stain vasculature with tomato lectin as

described in Chapter 3. We would then visualize the injected constructs relative to vasculature endothelial cells, allowing us to determine the BBB-crossing ability of the injected probes throughout the brain. The determination of BBB-crossing can also be accomplished independent of solving the global cardiovascular effect.

We have outlined the areas of study that would help to move this work forward and to further characterize vasoprobes as a potential readout of blood-brain barrier permeability by antibody-based conjugates targeted to the brain. If successful, this technique would simplify drug development targeted to the brain and would remove the need to extract the brain to access delivery of new drugs and the effectiveness of new delivery vehicles alike.

Methods

In vitro assessment and expression of Maxadilan-based contrasts. These methods were performed as previously described in Chapter 4 of Dr. Adrian Slusarczyk's thesis[6].

Animal procedures. All animal procedures were conducted in accordance with National Institutes of Health guidelines and with the approval of the MIT Committee on Animal Care. All experiments were performed with male Sprague-Dawley rats, age 7–9 weeks, supplied by Charles River Laboratories (Wilmington, MA).

Magnetic Resonance Imaging (MRI). Fourteen Sprague-Dawley rats were used for *in vivo* MRI experiments. Data were acquired on a 7 T 20 cm inner diameter, horizontal bore magnet (Bruker BioSpin MRI GmbH, Ettlingen, Germany).

Surgery for assessment of vasoactive probe injection. Six rats underwent surgery to implant bilateral cannula guides and two rats underwent surgery to implant headpost alone for positioning in the cradle during MRI scans. The rats were inducted using 3% isoflurane (ISO) anesthesia and maintained using 2% ISO with vacuum suction turned on to remove excess anesthetic. The rats were injected subcutaneously with 1.2 mg/kg of sustained release buprenorphine for analgesia. The rats' eyes were covered with paralube vet ointment (Dechra Veterinary Products, Overland Park, KS) to prevent eyes from drying from exposure to ISO. The rats' heads were shaved and cleaned with alcohol and povidone-iodine prep pads for easy access to the skull. Using sterile surgical equipment, the skin over the skull was retracted and the skull cleaned of tissue so that the sutures on the skull were clearly visible. The holes were drilled through the skull for the cannula guides bilaterally equidistant to midline. A small 26 GA needle was used to puncture the dura in each of the drilled holes, allowing smooth access to the brain parenchyma. The holes were air dried and bilateral connected custom-made cannula guides (22 GA PEEK, 6mm distance between the guides, Plastics One Inc, Roanoke, VA) were inserted into the holes. The guides were protruding 1 mm into the brain parenchyma. The guides were secured to the skull using white dental cement (C&B Metabond, Parkell, Edgewood, NY). Next, an in-house-made head post was attached to the rats' skulls posterior to the cannula guides implantation site using the white dental cement. After the

cement dried, the pink cold cure dental cement (Teets Denture Material, Patterson Dental, Saint Paul, MN) was applied over the white cement to secure the entire implant. Tissue glue was applied to seal the surface connecting the cement and skin areas around the implant. Cannula guides were sealed with dummy cannulas (protruding as far as the guide) to avoid exposure of brain tissue during the three-day recovery period.

MRI assessment of injected Maxadilan probes.

Experimental setup. Seven days after the implantation of the bilateral cannulas, six rats were imaged during Maxadilan intracranial infusion. For the imaging experiments, animals were anesthetized using 2% ISO in oxygen for induction. After numbing the trachea with lidocaine, the animals were intubated intratracheally using a 16 GA plastic part of the Surflash I.V. catheter (Terumo Medical Products, Somerset, NJ). The rats were then connected to a small animal respirator (Inspira Advanced Safety Ventilator; Harvard Apparatus, Holliston, MA), and fixed via their headposts into a custom built cradle for imaging with a commercial surface radiofrequency coil (Doty Scientific, Columbia, SC) fitting snugly around the headpost. Breathing rate and end-tidal expired isoflurane were continuously monitored. Once positioned in the cradle, the anesthesia was lowered to 0.75% ISO to allow for hemodynamic responses. Immediately before each experiment, two injection internal cannulas were attached to 25 µl Hamilton glass syringes and prefilled with the appropriate intracranial injection solution (aCSF or 100 nM Maxadilan in aCSF). Injection cannulas were then lowered, while applying positive pressure of 0.01 µl/min to avoid air bubbles, into the previously implanted bilateral cannula guides. Next, the Hamilton syringes were placed in a remote infuse/withdraw dual syringe pump (PHD

2000 Syringe Pump; Harvard Apparatus, Holliston, MA). Animals with their radiofrequency (surface and volume) coils (Doty Scientific, Columbia, SC) were inserted into the magnet bore and locked in a position such that the head of the animal was at the center of the magnet bore.

MRI and data analysis. Animals were scanned by MRI to measure the changes in hemodynamic contrast following intracranial injections. High resolution T_2-weighted anatomical scans of each animal were obtained using a rapid acquisition with relaxation enhancement (RARE) pulse sequence with echo time (TE) 44 ms, recycle time (TR) 2,500 ms, RARE factor 8, spatial resolution 100 μm x 100 μm x 1 mm, and matrix size 256 x 256. Hemodynamic contrast image series were acquired using a gradient echo planar imaging (EPI) pulse sequence with TE 17 ms, TR 4,000 ms, spatial resolution 390 μm x 390 μm x 1 mm, and matrix size 64 x 46. Five minutes of baseline measurement with 4 s per time point were acquired before probe infusion. Following this baseline period, while continuously collecting EPI scans, infusion pump was remotely turned on to commence intracranial injection (in the parenchymal tissue) of 1 μl aliquots of 100 nM Maxadilan or control solutions at the rate of 0.1 μl/min through the cannulas. EPI scans continued being collected for 15 minutes after the infusion of the Maxadilan probe has stopped for the total scan time of 30 minutes. MRI data was processed and analyzed using the AFNI software. The AFNI 3dAllineate command was used to align each animal's EPI data set to the corresponding RARE anatomical image. Each animal's image data were then aligned to the cannula tip of a reference anatomical MRI. We scaled each animal's data assigning the mean of the baseline time period to 100 using AFNI's 3dcalc command. To identify voxels with significant increases or decreases in BOLD signal, we

compared the signal of 5 minutes after the infusion to the baseline in the group concatenated data. For visualization, group signal change maps were overlaid on a reference anatomical image. The plateau percent signal change was determined by comparing signal values during baseline and after the infusion conditions over 1.2 x 1.2 mm regions of interest defined around cannula tip locations in individual animals' datasets and standard error was calculated across animals using MATLAB.

Semi-permanent tail vein catheter placement. Six anaesthetized rats underwent the placement of the tail vein catheter for BBB-crossing vasoactive construct injection in the MRI scanner. The tail vein was visualized by application of alcohol to the skin of the tail. A catheter (24 GA Surflo, Terumo, Somerset, NJ) was slowly inserted into the tail vein until clear blood back-flow was achieved. The catheter was secured to the tail by placing a tongue depressor (Puritan, Guilford, ME) underneath the tail and taping the tail and the tongue depressor together using surgical tape. The catheter was flushed with 0.5% heparin in PBS to prevent clotting and secured with a stopper until the contrast infusion in the MRI.

MRI assessment of BBB-crossing vasoactive constructs.

Experimental setup. Seven days after headpost implantation as described above, two rats were imaged during I.V. infusion of BBB-crossing FC5-Maxadilan construct vs control. For the imaging experiments, animals were anesthetized using 2% ISO in oxygen for induction. After numbing the trachea with lidocaine, the animals were intubated intratracheally using a 16 GA plastic part of the Surflash I.V. catheter (Terumo Medical

Products, Somerset, NJ). The rats were then connected to a small animal respirator (Inspira Advanced Safety Ventilator; Harvard Apparatus, Holliston, MA), and fixed via their headposts into a custom built cradle for imaging with a commercial surface radiofrequency coil (Doty Scientific, Columbia, SC) fitting snugly around the headpost. Breathing rate and end-tidal expired isoflurane were continuously monitored. Once positioned in the cradle, the anesthesia was lowered to 0.75% ISO to allow for hemodynamic responses. Immediately before each experiment, the I.V. tail vein injection catheter was attached via tubing to a plastic syringe and was prefilled with the appropriate I.V. injection solution (6 mg/ml of FC5-Maxadilan or PBS control). Next, the syringe was placed in a remote infuse/withdraw dual syringe pump (PHD 2000 Syringe Pump; Harvard Apparatus, Holliston, MA). Animals with their radiofrequency (surface and volume) coils (Doty Scientific, Columbia, SC) were inserted into the magnet bore and locked in a position such that the head of the animal was at the center of the magnet bore.

MRI and data analysis. Animals were scanned by MRI to measure the changes in hemodynamic contrast following intracranial injections. High resolution T_2-weighted anatomical scans of each animal were obtained using a rapid acquisition with relaxation enhancement (RARE) pulse sequence with echo time (TE) 44 ms, recycle time (TR) 2,500 ms, RARE factor 8, spatial resolution 100 μm x 100 μm x 1 mm, and matrix size 256 x 144. Hemodynamic contrast image series were acquired using a T_2*-weighted RARE pulse sequence with effective TE 44 ms, TR 2222 ms, spatial resolution 200 μm x 200 μm x 1 mm, and matrix size 128 x 72. Ten minutes of baseline measurement with 1 min per time point were acquired before probe infusion. Following this baseline period, while continuously collecting time series scans, infusion pump was remotely turned on to

commence I.V. injection of 1 ml of 6 mg/kg FC5-Maxadilan or control solutions at the rate of 0.2 ml/min through the tail vein catheter. Time series scans continued being collected for 75 minutes after I.V. infusion of the BBB-crossing Maxadilan probe has stopped for the total scan time of 90 minutes. MRI data was processed and analyzed using the AFNI software. We scaled each animal's data assigning the mean of the baseline time period to 100% using AFNI's 3dcalc command. To identify voxels with significant increases or decreases in BOLD signal, we compared the signal from end of time series to the baseline for each animal. For visualization, signal change maps were overlaid on a reference anatomical image. The time courses from the entire brain were plotted for both the BBB-crossing construct and the control injections.

Heart rate monitoring following administration of vasoactive peptides. Four rats were injected with varying concentrations of vasoprobes I.V. while monitoring and recording the heart rate before and after the injection. CGRP was used as vasoprobe for these experiments due to its affordability and ease of purchase. The animals were anesthetized using 0.75% ISO to allow for hemodynamic changes as would be the case during vasoprobe injections in the MRI scanner. One ml of 2 mM or 2 μM CGRP or saline control were injected I.V. at 0.2 ml/min through a semi-permanent catheter. The heart rate was monitored and recorded 10 minutes prior the injection, during the injection and for 15 minutes after the injection.

References

1. Daneman, R. & Prat, A. The blood-brain barrier. *Cold Spring Harb. Perspect. Biol.* **7**, a020412 (2015).
2. Banks, W. A. Characteristics of compounds that cross the blood-brain barrier. *BMC Neurol.* **9**, S3 (2009).
3. Pardridge, W. M. Drug and gene targeting to the brain with molecular Trojan horses. *Nat. Rev. Drug Discov.* **1**, 131–139 (2002).
4. Niewoehner, J. *et al.* Increased brain penetration and potency of a therapeutic antibody using a monovalent molecular shuttle. *Neuron* **81**, 49–60 (2014).
5. Joosten, L. *et al.* Preclinical evaluation of PAC1 targeting with radiolabeled Maxadilan. *Sci. Rep.* **7**, (2017).
6. Slusarczyk, A. L. (Adrian L. Molecular imaging with engineered physiology. (Massachusetts Institute of Technology, 2016).
7. Moro, O. *et al.* Functional Characterization of Structural Alterations in the Sequence of the Vasodilatory Peptide Maxadilan Yields a Pituitary Adenylate Cyclase-activating Peptide Type 1 Receptor-specific Antagonist. *J. Biol. Chem.* **274**, 23103–23110 (1999).
8. Farrington, G. K. *et al.* A novel platform for engineering blood-brain barrier-crossing bispecific biologics. *FASEB J. Off. Publ. Fed. Am. Soc. Exp. Biol.* **28**, 4764–4778 (2014).
9. Lajoie, J. M. & Shusta, E. V. Targeting receptor-mediated transport for delivery of biologics across the blood-brain barrier. *Annu. Rev. Pharmacol. Toxicol.* **55**, 613–631 (2015).
10. Muruganandam, A., Tanha, J., Narang, S. & Stanimirovic, D. Selection of phage-displayed llama single-domain antibodies that transmigrate across human blood-brain barrier endothelium. *FASEB J. Off. Publ. Fed. Am. Soc. Exp. Biol.* **16**, 240–242 (2002).
11. Abulrob, A., Sprong, H., Van Bergen en Henegouwen, P. & Stanimirovic, D. The blood-brain barrier transmigrating single domain antibody: mechanisms of transport and antigenic epitopes in human brain endothelial cells. *J. Neurochem.* **95**, 1201–1214 (2005).
12. Webster, C. I. *et al.* Brain penetration, target engagement, and disposition of the blood-brain barrier-crossing bispecific antibody antagonist of metabotropic glutamate receptor type 1. *FASEB J. Off. Publ. Fed. Am. Soc. Exp. Biol.* **30**, 1927–1940 (2016).
13. Haqqani, A. S. *et al.* Multiplexed evaluation of serum and CSF pharmacokinetics of brain-targeting single-domain antibodies using a NanoLC-SRM-ILIS method. *Mol. Pharm.* **10**, 1542–1556 (2013).
14. Girard, B. M., Malley, S. E., Mathews, M. M., May, V. & Vizzard, M. A. Intravesical PAC1 Receptor Antagonist, PACAP(6-38), Reduces Urinary Bladder Frequency and Pelvic Sensitivity in NGF-OE Mice. *J. Mol. Neurosci. MN* **59**, 290–299 (2016).
15. Mankarious, S. *et al.* The half-lives of IgG subclasses and specific antibodies in patients with primary immunodeficiency who are receiving intravenously administered immunoglobulin. *J. Lab. Clin. Med.* **112**, 634–640 (1988).

16. Spector, R. & Mock, D. Biotin transport through the blood-brain barrier. *J. Neurochem.* **48**, 400–404 (1987).
17. Joo, K. M. *et al.* Distribution of vasoactive intestinal peptide and pituitary adenylate cyclase-activating polypeptide receptors (VPAC1, VPAC2, and PAC1 receptor) in the rat brain. *J. Comp. Neurol.* **476**, 388–413 (2004).